

Search for narrow states by detection of monochromatic gamma rays in $\bar{p}p$ annihilation at rest

M. Chiba,^f K. Doi,^e T. Fujitani,^e J. Iwahori,^{a,*} M. Kawaguti,^a M. Kobayashi,^c
M. Koike,^b T. Kozuki,^c S. Kurokawa,^c H. Kusumoto,^{e,†} H. Nagano,^e Y. Nagashima,^e T. Omori,^{e,‡}
S. Sugimoto,^e M. Takasaki,^c F. Takeuchi,^d M. Tsuchiya,^e M. Ueda,^e Y. Yamaguchi,^e and H. Yoshida^a

^a*Faculty of Engineering, Fukui University, Fukui 910, Japan*

^b*Institute for Nuclear Study, University of Tokyo, Tanashi, Tokyo 188, Japan*

^c*National Laboratory for High Energy Physics (KEK), Tsukuba-gun, Ibaraki-ken 305, Japan*

^d*Faculty of Science, Kyoto Sangyo University, Kita, Kyoto 603, Japan*

^e*Physics Department, Osaka University, Toyonaka, Osaka 560, Japan*

^f*Physics Department, Tokyo Metropolitan University, Setagaya, Tokyo 152, Japan*

(Fukui-INS-KEK-Kyoto Sangyo-Osaka-Tokyo Metropolitan Collaboration)

(Received 15 May 1987)

We measured inclusive γ -ray spectra from $\bar{p}p$ annihilation at rest to search for narrow γ lines associated with the production of baryonia. The measurement was done with statistics several times as high as those of earlier experiments by using modularized NaI(Tl) detectors. We have not observed any narrow states, i.e., baryonium candidates, with statistical significance higher than 4σ . The 4σ upper limits for the yield of $\bar{p}p \rightarrow \gamma B$ times the decay branching ratio of B into N_{ch} -prong states is $(1.2-0.2) \times 10^{-3}$ at γ -ray energy of 80–938 MeV for the sum over N_{ch} , $(0.3-0.1) \times 10^{-3}$ for each of $N_{\text{ch}}=0$ and ≥ 6 , and $(0.8-0.1) \times 10^{-3}$ for each of $N_{\text{ch}}=2$ and 4. At 2 to 3σ levels, however, we have seen nine narrow γ -ray peaks with individual yields between 10^{-4} and 10^{-3} for various charge multiplicities.

I. INTRODUCTION

It is believed that all hadrons are made of quarks (q), antiquarks (\bar{q}), and gluons (g). All the well-established mesons and baryons can be simply assigned to colorless states of $(\bar{q}q)$ and (qqq) , respectively. As there is no clear reason why exotic states such as $(\bar{q} \bar{q} q q)$, $(qqq \bar{q} q)$, (gg) , etc., should not exist, the search for them has long been one of the most interesting subjects in hadron physics. The existence or nonexistence of these objects could shed light on the limits of quantum chromodynamics (QCD).

Historically, the existence of exotic states consisting of diquark (qq) and an antidiquark ($\bar{q} \bar{q}$), now called baryonia, was first predicted in the dual-model description of hadron interactions.¹ Their existence has also been expected² in many quark models. The quark configuration in baryonia indicates that they must be closely coupled to baryon-antibaryon states. Baryonia above twice the nucleon rest mass have been extensively searched in formation experiments, such as $\bar{p}p \rightarrow$ baryonia (B) $\rightarrow \bar{p}p$, $\bar{n}n$, mesons, etc., and in production experiments, such as $\pi p \rightarrow B +$ hadrons with B decaying into $\bar{p}p$. The most well-known candidate, a narrow resonance $S(1932)$, has been examined in many experiments. As a result, the signal has become weak and the S has not yet been confirmed. Also, none of the other wider resonances have as yet been established.³

For the baryonia below twice the nucleon rest mass, the situation is a little different. Even if $(\bar{q} \bar{q} q q)$ baryonia should not exist, atomic nucleon-antinucleon bound states⁴ may exist owing to a strong attractive force arising

from ω meson exchange. One of the best places to look for baryonia below the two-nucleon threshold, including atomic $\bar{N}N$ bound states, is $\bar{p}p$ annihilation at rest. A baryonium B may be produced in the reaction of $\bar{p}p \rightarrow \gamma B$ (or πB) with an accompanying monochromatic γ ray (or π meson). As the B has insufficient energy to decay into $\bar{N}N$ in this reaction, the B should have a very narrow width. In an experiment⁵ at the CERN Proton Synchrotron, six monochromatic lines were observed in the inclusive γ -ray spectrum with an individual yield of $(1-3) \times 10^{-3}$ per annihilation at 2 to 3σ levels. Four of them at M_B (=mass of B in MeV/c^2) = 1771, 1694, 1638, and 1210 were observed at the same energies as in the previous measurements⁵ which had been carried out by the same group, though the yields observed in the experiment of Ref. 5 were smaller than those in the previous measurements. The $m_B=1771$ peak was also observed⁶ in another experiment at Brookhaven National Laboratory (BNL) with a yield of 6×10^{-3} at a statistical significance level of 3σ . A calculation⁷ based on a quark potential model for $(\bar{q} \bar{q} q q)$ baryonium production accompanied by the emission of an energetic photon, however, predicts yields $\sim 10^{-4}$, which are smaller than the above observed values by an order of magnitude. According to Ref. 7, the observed bumps should be then more naturally explainable as $\bar{N}N$ bound states rather than as diquonium signals. The evidence for the monochromatic γ lines is, however, controversial^{5,6} and confirmation of the result of Ref. 5 is needed.

As for strong-interaction transitions from $(\bar{p}p)$ atoms to baryonia, two experiments were carried out at CERN Low Energy Antiproton Ring (LEAR) in search for

monochromatic charged pions. A Greece-USA group⁸ did not observe any baryonium candidates, giving an upper limit of 0.2×10^{-3} (90% C.L.) for the yields of narrow states in a limited mass range of $m_B = 1510$ – 1660 . The ASTERIX Collaboration⁹ studied $\bar{p}p$ annihilation from the initial atomic angular-momentum $L=1$ state by using a hydrogen gas target. Selection of the $L=1$ state was different from all the other experiments discussed thus far, in which the initial state was largely the $L=0$ state.¹⁰ Ahmad *et al.*⁹ did not observe any narrow lines, giving a 5σ upper limit of 2×10^{-3} in a mass range of $M_B = 1100$ – 1670 .

The measurement of γ (and also π^0) transitions has an advantage that it is sensitive to both isoscalar and isovector baryonia, while the measurement of charged-pion transitions is sensitive only to isovector baryonia. The measurement of γ transitions has, in comparison with that of π^0 transitions, another advantage in that it is sensitive to baryonia with masses close to the two-nucleon mass threshold. Inclusive γ -ray spectra, however, suffer from a huge background from π^0 decay. In order to detect tiny monochromatic γ -ray peaks whose individual yields are of order 10^{-4} per annihilation, high statistics and good energy resolution for γ -ray measurement are of vital importance. In addition, removal of fake peaks is also essential. In order to remove fake or spurious events, which come from erroneous registration of minimum-ionizing particles as γ rays, annihilation of antiprotons outside the liquid-hydrogen cell, coincidence of cosmic rays and antiproton annihilation, etc., it is important to track all charged particles and to reconstruct the vertex point for each event. Putting the main emphasis on the above points, we have measured¹¹ inclusive γ -ray spectra in $\bar{p}p$ annihilation at rest in experiment E68 at the KEK 12-GeV Proton Synchrotron.

II. EXPERIMENTAL SETUP

A. General

With the requirements described above as a guideline, we have constructed a detector consisting of the following major components (see Figs. 1 and 2).

(1) A segmented NaI(Tl) calorimeter^{12,13} for γ rays. An array of 6 (along the beam) \times 16 (azimuthally) NaI(Tl) modules were assembled in a half-barrel configuration with the barrel axis along the beam and shielded with a wall of scintillating glass.^{14,15}

(2) Cylindrical multiwire proportional chambers¹⁶ (MWPC's) as the main tracking device. Both ends of the cylinder were closed with flat MWPC's.

(3) Counter hodoscopes made of plastic scintillators. They were used to trigger events, to help track charged particles, and to help identification of γ rays in the NaI.

(4) Small round-shaped MWPC's and a Si solid-state detector (SSD) mounted inside the cylindrical MWPC's. They were used to determine the trajectories and momenta, respectively, of slow projectile antiprotons.

The above detector elements surrounded a 3.3-liter liquid-hydrogen cell,¹⁷ in which almost all incident antiprotons stopped.

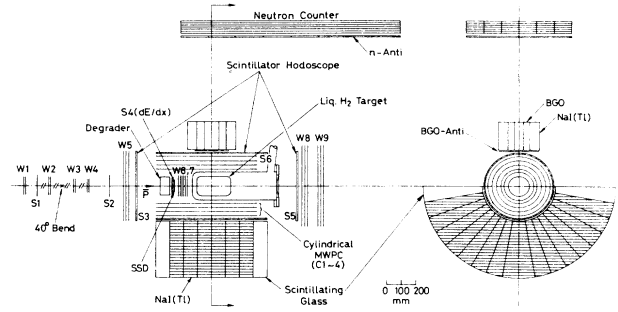


FIG. 1. Experimental setup. $S1$ – $S6$ are plastic scintillators, $W1$ – $W9$ flat MWPC's, and $C1$ – $C4$ cylindrical MWPC's. The barrel hodoscope $S6$ consists of 36 scintillator slabs, each slab subtending 10 degrees azimuthally.

B. Setup

Incoming antiprotons at 580 MeV/c were selected by the time of flight (TOF) between two scintillation counters $S1$ (2 mm thick) and $S2$ (10 mm thick) separated by 6.34 m, and tracked with four small MWPC's, $W1$ – $W4$, each consisting of two wire planes x and y . Here x and y denote position measurement along the horizontal and vertical axes, respectively. The antiprotons were then slowed down in a 66-mm-thick graphite degrader (13.2 g/cm^2). Immediately downstream of the degrader, dE/dx of the slow antiprotons was measured with a 10-mm-thick plastic scintillator $S4$ for fast electronics and with a 3-mm-thick Si SSD of 90 mm in diameter for off-line analysis (see Fig. 2). The $S4$ was ap-

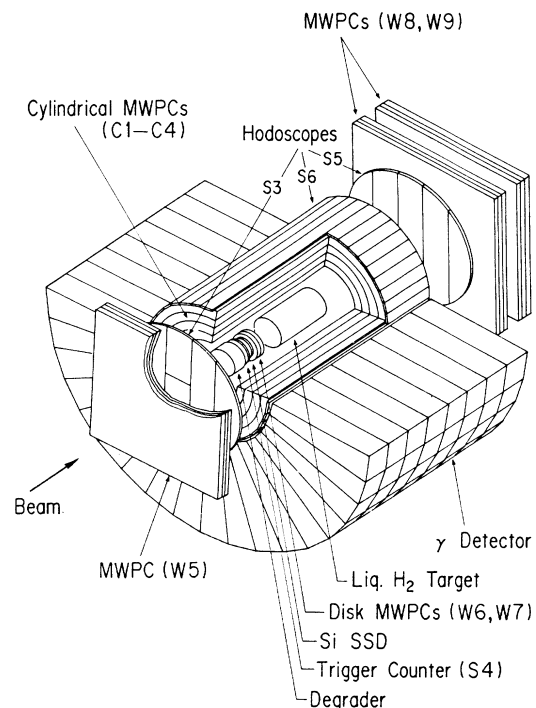


FIG. 2. A conceptual sketch of the heart of the detector.

proximately round shaped and viewed by six photomultipliers (Hamamatsu R1232) through light guides on the circumference in order to obtain good uniformity with respect to position (see Figs. 3 and 4). The trajectories of slow antiprotons were measured with the round-shaped MWPC's *W6* and *W7* (the sensitive area being 150 mm in diameter, see Fig. 3), which consisted of six planes in total x, y, v, x, y, u . Here the direction of u (v) was inclined by 45° (-45°) with respect to y . The antiprotons finally stopped in the liquid-hydrogen cell.

The liquid-hydrogen cell¹⁷ was 140 mm in diameter and 230 mm in length corresponding to the range of 330-MeV/ c antiprotons. It was constructed of a 0.2-mm-thick welded stainless-steel sheet. The cell sat on the beam line in a vacuum envelope of aluminium, which was 2 mm thick at the beam entrance and 3 mm thick at the cylindrical walls.

Secondary charged particles were measured by scintillator hodoscopes and MWPC's. The barrel scintillator hodoscope consisted of 36 plastic scintillator (NE110) slabs of 10 mm thickness, each slab subtending 10° azimuthally around the beam axis (see Fig. 5). The barrel was closed with two planar round-shaped hodoscopes *S3* and *S5*, each consisting of five scintillator slabs of 10 mm thickness and 100 mm width (see Fig. 5). The hodoscopes served to count the charged-particle multiplicity for fast trigger logic.

Inside the barrel hodoscope were mounted four layers of coaxial cylindrical MWPC's, *C1*–*C4* (Ref. 16), with a sensitive area of 684 mm along the axis and with an anode wire spacing of 4 mm. In addition to the conventional anode readout, the cathode readout was also incorporated in the innermost (*C1*) and the outermost (*C4*) MWPC's to obtain longitudinal track positions. To improve the position resolution, the cathode strips were wound helically in the inverse direction for the inner and the outer cathode planes. The cathode pulse height was read out for every 12-mm spacing, i.e., a sum of two cathode strips, by LeCroy 2285 analog-to-digital converters (ADC's) to obtain longitudinal track posi-

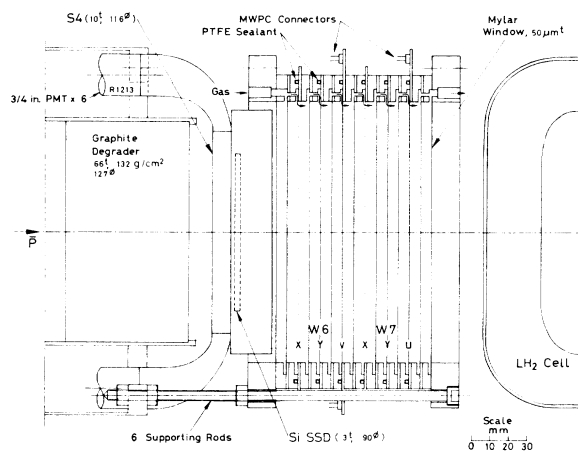


FIG. 3. A sketch of the setup immediately upstream of the hydrogen target, including the dE/dx counter *S4*, the Si SSD and the round-shaped MWPC's *W6*–*W7*.

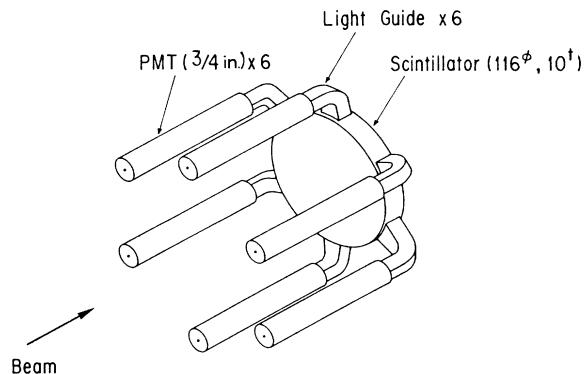


FIG. 4. A conceptual sketch of the dE/dx counter *S4* (see the text).

tions. Three sets of flat MWPC's in total were mounted on both ends of cylindrical MWPC's; each set read out x, y , and u (or v). The anode wire spacing was again 4 mm. The total geometrical acceptance of the cylindrical plus the flat MWPC's for tracking secondary charged particles was about 93% of 4π sr. All the MWPC's, except the beam MWPC's *W1*–*W4*, were operated in a gas mixture of argon (62%), isobutane (30%), and methylal (8%) at a flow rate of $100 \text{ cm}^3/\text{min}$. For *W1*–*W4*, a small amount of freon (0.6%) was added to make the MWPC's stable against high-intensity beams.

γ rays were measured with a NaI(Tl) calorimeter¹² shielded with a scintillating glass wall. The 96 NaI and 48 scintillating glass modules were assembled into a half-barrel with an inner radius of 25 cm. The NaI covered a solid angle of 22% of 4π sr. Each NaI module had a shape of a truncated trapezoidal pyramid

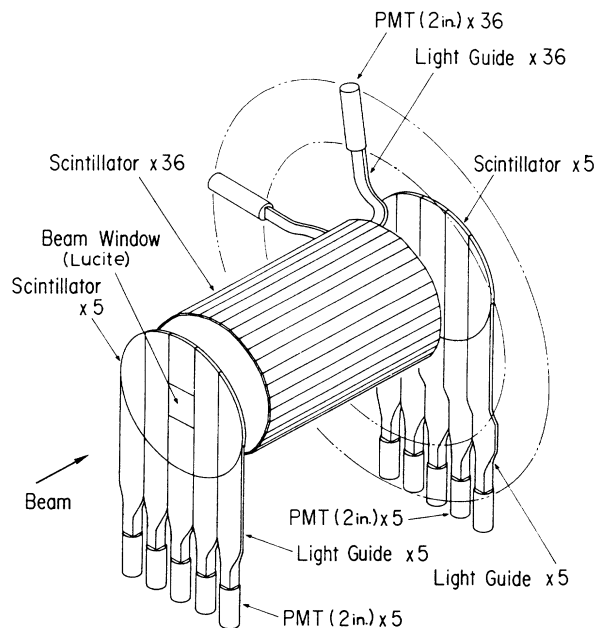


FIG. 5. A conceptual sketch of the scintillator hodoscopes (see the text).

of $(43.74 \times 94) \times (109.71 \times 94) \times 377 \text{ mm}^3$ ($15X_0$ long). Each scintillating glass module had the same shape as the NaI, except for its depth of 400 mm ($9.3X_0$). Each γ module was read out with a 3-in. photomultiplier (Hamamatsu, R594), whose output was clipped with a 100-m-long cable (50Ω) terminated by a $20\text{-}\Omega$ resistor. The scintillating glass^{14,15} was used to measure the shower leakage from the NaI. If the leakage exceeded a certain fraction (typically 10%) of the γ energy, the γ ray was rejected in off-line analysis. Otherwise, the energy deposits in the scintillating glass were added to those in the NaI.

Throughout the experiment, the temperature of the detector room (or the surface of the calorimeter) was kept constant (20°C) within $\pm 2^\circ\text{C}$ (or $\pm 1^\circ\text{C}$).

C. Antiproton beam

The $K4$ beam¹⁸ has been newly constructed with its upstream half shared with the existing $K3$ beam. Owing to its characteristic features of a large length (28.5 m) and double-stage mass separation, the $e\mu\pi/\bar{p}$ ratio was roughly 8 at $580 \text{ MeV}/c$, i.e., an order of magnitude smaller than in ordinary \bar{p} beam lines equipped with single-stage mass separation.

The stopping rate of antiprotons in the liquid-hydrogen cell was maximum at the beam-line momentum of $580 \text{ MeV}/c \pm 3\%$, where 510 antiprotons were obtained per 10^{12} protons on the production target. The antiprotons were slowed down in a graphite degrader, and more than 45% of the $580\text{-MeV}/c$ antiprotons stopped or annihilated in flight in the liquid-hydrogen target. The average stopping rate during the experiment was 270 per 1.2×10^{12} protons per pulse. The beam spill was 300 ms at the repetition of 0.4 Hz.

D. Gamma detector

The energy resolution of a 5×5 modular array of NaI(Tl) was measured for an electron beam injected along the central axis of the array. The full width at half maximum (FWHM) resolution was $3.6\% / (E_e \text{ in GeV})^{1/4}$, where E_e is the electron energy (see Fig. 6). The resolution of the whole calorimeter in the final setup was measured for 129-MeV γ rays (Panofsky γ) produced by a π^- beam stopping in the liquid-hydrogen cell. In this measurement, the incident γ rays uniformly illuminated the front face of the calorimeter in the same way as in the experiment. The obtained resolution of 8.9% (see Fig. 7) is plotted in Fig. 6 with an open circle. This gives

$$\Delta E/E = 5.3\% / (E \text{ in GeV})^{1/4}, \quad (1)$$

when we assume a law of the inverse fourth root of γ energy, E . In the above measurement, the γ energy was obtained by summing all NaI modules because the final state had only a few particles ($\pi^- p \rightarrow \pi^0 n, \gamma n$). In the actual $\bar{p}p$ experiment, however, summation over the NaI modules has to be local because many particles other than the γ ray may fall on the NaI. Consequently, a cluster logic, to be described later in Sec. V, was applied

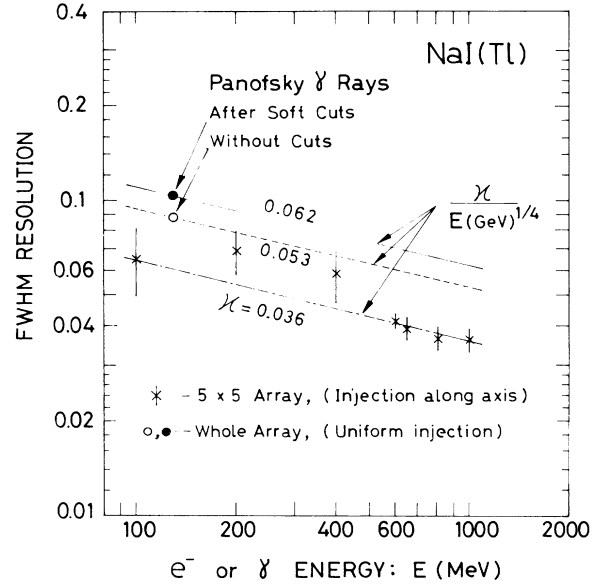


FIG. 6. Energy resolution of the NaI(Tl) calorimeter. Crosses show the resolution obtained in a 5×5 array of modules for a pencil beam of electrons injected along the central axis of the array. The chained line is a fit by $\kappa[E(\text{GeV})]^{-1/4}$ with a constant $\kappa = 0.036$. Open and solid points show the resolution of the whole calorimeter for 129-MeV γ rays illuminating the front face uniformly (see the text). The statistical as well as systematic errors of these points are small (within the points). The broken and the solid lines show Eqs. (1) and (2), respectively. The solid line was adopted as the overall instrumental resolution.

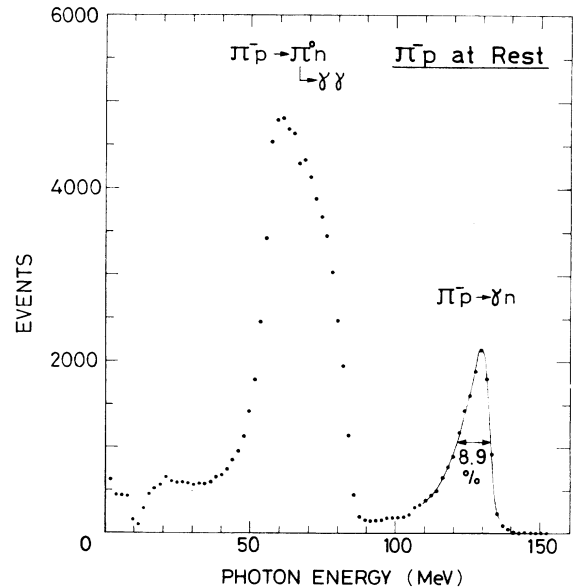


FIG. 7. A typical energy spectrum of γ rays produced by a π^- beam stopping in the liquid-hydrogen target. The beam line was tuned for $167 \text{ MeV}/c \pi^-$. Neutral events were triggered when one or two γ rays fell on the NaI.

to the off-line analysis to isolate each γ ray from neighboring particles. When the cluster logic was applied to the π^- beam data, the FWHM energy resolution for 129-MeV γ rays was degraded to 10.4%, which is presented in Fig. 6 as a solid circle. From this number, allowing for error, we took the overall instrumental FWHM as

$$\Delta E/E = 6.2\% / (E \text{ in GeV})^{1/4} \quad (2)$$

for energies above 80 MeV, though this must be an overestimation at high energies. The actual resolution at higher energies will fall between Eq. (1) and Eq. (2) because the effect of the cluster logic (energy cut at 0.7 MeV) should be smaller at higher energies than at 129 MeV and also because the energy resolution in the NaI improves faster¹² than the inverse fourth-root law as the energy is increased from 100 to 1000 MeV.

The energy resolution of scintillating glass modules was measured with the same electron beam as for the NaI modules. The FWHM resolution in a typical module varied from 22% at 200 MeV/c to 11% to 1000 MeV/c (Ref. 12).

E. Multiwire proportional chambers (MWPC's)

The beam MWPC's ($W1-W4$) were of a standard type with metal flanges. The anode was a gold-plated tungsten wire 25 μm in diameter, stretched at a 2-mm spacing. The cathode was a 25- μm -thick polyester film plated with 10- μm -thick aluminum on both side (for $W1$ and $W2$) or a Be-Cu wire of 100 μm diameter (for $W3$ and $W4$). The anode to cathode gap was 6 mm.

$W6-W7$ were constructed in a configuration as sketched in Fig. 3. In order to have as large a sensitive area as possible in a limited space, both the outer contour and the sensitive area were round shaped. All six wire planes were stacked together between two narrow aluminum end flanges. The anode was similar to that for $W1-W4$, and the cathode was similar to that for $W1$ and $W2$. The anode to cathode gap was again 6 mm. The efficiency of each wire plane was higher than 99% during the experiment.

It is desirable to construct the cylindrical MWPC's ($C1-C4$) without using any massive supporting rods over the sensitive volume because massive material, especially when distributed locally in space, may damage the reliability of a search for tiny narrow structures in γ -ray spectra. Each MWPC was self-supported by the inner and outer cathode cylinders of light mass.¹⁶ Each cylinder was made of approximately 6-mm-thick aramid fiber/phenolic resin honeycomb sandwiched between 50- μm -thick Kapton sheets, to which cathode electrodes (35- μm -thick copper) were laminated. The chamber mass was about 160 mg/cm² for each of $C1-C4$. The anode to cathode gap was 6.5 mm and gold-plated tungsten wires of 25 μm diameter were stretched for the anode.

In an electron-beam test, the anode efficiency was higher than 99% over the whole sensitive area in each of $C1-C4$ with the high voltage set at the plateau, whose width was more than 300 V. The anode efficiency versus high-voltage characteristics was independent of the posi-

tion within a shift of 100 V. The cathode efficiency was higher than 99% in the anode plateau region. During the experiment, however, the anode efficiency averaged over $C1-C4$ was degraded to 95%, and the cathode efficiency to 91%, because of larger electronic noises than during the test. The position resolution (1σ) along the anode wire (i.e., along the longitudinal direction) was found to be 0.6 mm when the hit position perpendicular to the cathode strips was given by the center of gravity of the pulse-height distribution over the neighboring strips.

The large flat MWPC's, $W5$, $W8$, and $W9$ were also constructed by employing a similar honeycomb structure for the mechanical support without any metal flanges. This method was adopted in order to minimize the acceptance gap for tracking by making the MWPC's smaller and thinner in the outer size and by mounting them as close to the cylindrical MWPC's as possible. The three MWPC's had a similar structure: each consisted of three anode planes with the wire directions along x , y , and u (or v). Each MWPC had a configuration of $HGAGHGAGHGAGH$ along the thickness, where H denotes a 6-mm-thick aramid fiber/phenolic resin honeycomb sandwiched between 50- μm -thick Kapton sheets laminated with 35- μm -thick copper electrodes for the cathode, G a 6.0-mm-thick and 15-mm-wide $G10$ frame creating the anode to cathode gap, and A the anode wire plane. The same wires as in cylindrical MWPC's were used at a wire spacing of 4 mm. The mass of each chamber was about 320 mg/cm². The anode efficiency was higher than 99% during the electron beam test, while during the experiment it was 96%, on the average of the three planes, in $W5$, 91% in $W8$, and 95% in $W9$.

III. GAIN CALIBRATION AND MONITORING OF CALORIMETER

Since we searched tiny narrow peaks sitting on a huge background, precise calibration as well as gain monitoring of γ detectors was vitally important. The widths of the peaks have been estimated to be of order 10 MeV or less,^{2,7} which is smaller than the instrumental width of the present calorimeter. As the instrumental width (1σ) was 2.6% (4.0%) for isolated γ rays of 500 (100) MeV without any software cuts, we required better than 1% accuracy in both the calibration and the monitoring. To achieve this goal, we not only took care of the accuracy in each task, but also prepared a redundancy.

A. Excitation curves

The excitation curve of each γ module was measured for electrons at the $T1$ test beam at four energies of 200, 400, 650, and 900 MeV. A pencil beam of electrons, identified with a gas Cherenkov counter, was injected along the axis of each γ module. The pulse-height spectrum showed a small left-right asymmetry owing to shower leakage. As the asymmetry was nearly independent of energy, we took its mean over different energies and over many modules. We employed this mean asymmetry in fitting the pulse-height spectrum. Saturation of the pulse height of the NaI modules, which amounted to

5% at 650 MeV on the average of all the modules, was corrected for in the off-line analysis. For this purpose, the excitation curve of each module was fitted with a straight line at low energies smoothly connected to the sum of the straight line plus a hyperbolic tangent term at high energies. After the correction for the saturation, the energy deposit in a single module was still smaller than the beam energy owing to shower leakage. We corrected for the energy containment by using a Monte Carlo calculation based on the EGS program:¹⁹ the energy deposit in a single module is about 89%, which is constant within $\pm 1\%$, independent of the energy between 10 and 1000 MeV. A small ambiguity in the absolute energy scale of the test beam was not important because the absolute energy calibration was carried out during the experiment as described in the following paragraph. The scintillating glass modules were simpler than the NaI ones because saturation was absent (less than 1%) over the whole energy range tested.

B. Gain calibration

Intercalibration of the gains of the NaI modules was carried out in two different methods. In the one method, 200-MeV/c electrons, to which the K4 beam was tuned, were injected along the axis of each γ module one by one. For each γ module, electronic circuits such as an ADC, a signal divider, a variable attenuator, coaxial cables, a high-voltage source, etc., were the same as in the experiment. All the gain monitors as described later were recorded during the calibration.

In the other method, the calibration was done during the experiment by measuring the 129-MeV γ rays (Panofsky γ) from π^-p at rest into γn . This was done about once a month by switching the beam to 167-MeV/c negative pions, which stopped in the liquid-hydrogen target. As the γ rays illuminated all the γ modules uniformly, we summed signals from many neighboring modules to obtain the γ energies. The calibration coefficients of all the γ modules were determined by solving a set of linear equations, so that the rms deviation of the measured energies from 129 MeV should be minimum.

The module gains obtained by the both methods agreed with each other within 2% for most of the NaI modules sitting in the longitudinally central layers. For the NaI modules in the longitudinally peripheral layers, their calibration coefficients (in MeV per ADC channel) were systematically larger by about 4% with the Panofsky γ rays than with the electron beam. This difference can be qualitatively interpreted in terms of energy absorption in the module walls, which will be larger when γ rays enter peripheral modules with large angles. However, the difference is expected to be unimportant, because the longitudinally peripheral modules are less important than the central ones. If γ rays should dominantly deposit energies in the peripheral NaI modules, most of such γ rays will deposit a sizable fraction of the energy in the surrounding scintillating glass, and will then be rejected. As the calibration condition with the Panofsky γ rays is similar to the experimental condition, the calibration coefficients obtained with this method

were used. There are additional reasons why we preferred the calibration with the Panofsky γ rays: the definite energy of the Panofsky γ rays enables not only relative but also absolute energy calibration, and the calibration can be easily repeated during the experiment in order to examine the stability of the calibration coefficients.

Reliability of the calibration coefficients was estimated by comparing them at different times. When drifts in module gains (to be described later in more detail) were corrected for, the calibration coefficients measured at different times remained the same within $\pm 1\%$ for most of the central 4×14 NaI modules (see Fig. 8). The larger scattering of $\pm 5\%$ observed for the peripheral modules (see Fig. 8) is not important because it may be partly due to poor statistics in the measurement and because the peripheral modules are again less important than the central ones as described in the previous paragraph.

The absolute energy scale was determined to within 2% from the 129-MeV γ rays produced in $\pi^-p \rightarrow \gamma n$, and from 780-MeV π^0 mesons in $\bar{p}p \rightarrow \pi^0 p^0 / \omega$. The 780-MeV π^0 peak arose in the γ -ray spectra because some of the 2γ rays from π^0 decay were registered as single γ rays, as described in more detail in Sec. VI.

C. Gain monitoring

The photomultiplier gains were periodically monitored with an accuracy better than $\pm 1\%$ (Ref. 20) by using two independent systems of xenon flash lamps as sketched in Fig. 9. The monitoring system was based on (i) use of xenon lamps as a light source with a continuous spectrum and (ii) use of photodiodes as stable monitoring devices for the light intensity. Pulse-to-pulse fluctuations in each xenon lamp (EG&G, FX124) were directly monitored with three photodiodes (Hamamatsu,

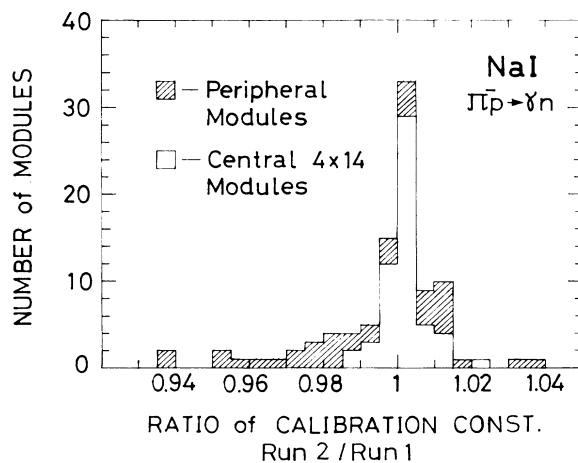


FIG. 8. Reproducibility of calibration coefficients for the NaI modules in two measurements carried out before and after an interval of about one month. The calibration coefficients were determined each time with the 129-MeV γ rays from π^-p at rest and corrected for the drifts in the module gains, which were monitored by the xenon lamp systems.

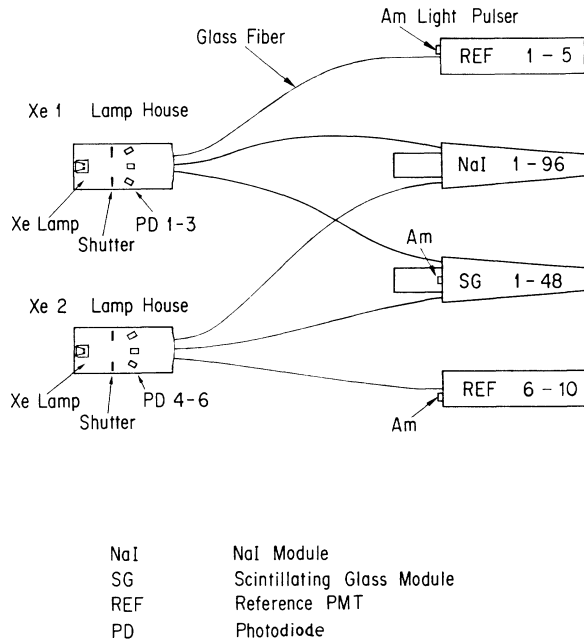


FIG. 9. Gain monitoring system for the NaI and the scintillating glass modules.

S1227) mounted in the lamp house and also by five references 3-in. photomultipliers (Hamamatsu, R594) via optical fibers. The reference photomultipliers were again monitored with radioactive NaI(Tl)-Am light pulsers.²¹ Some of the reference photomultipliers were placed inside a constant-temperature box stabilized to within $\pm 1^\circ\text{C}$. The light was distributed to all the γ modules one by one via quartz glass fibers. Each fiber was 4 m long and $400\ \mu\text{m}$ (or $133\ \mu\text{m}$) in diameter for the NaI modules (or the scintillating glass modules as well as the reference photomultipliers).

While the xenon lamps were flashed constantly at 10 Hz, a shutter was closed in the lamp house except in xenon lamp monitoring runs. The pulse height and width were made similar to those of NaI signals by adjusting the operating condition for the xenon lamps (high voltage of 850 V and triggering voltage of 140 V). The decay of the light intensity, as measured by photodiodes, was less than 1% per month (2.6×10^7 pulses).

The gain monitoring was done once to twice a day throughout the experiment. Photodiodes were found to be mutually stable within 0.3% (Refs. 12 and 20) with respect to the pulse height. Gain drifts in the γ modules were then determined with the photodiodes as the reference. The gain drift averaged over the 96 NaI modules was 2% per month, while that over the 48 scintillating glass ones was 1.1% per month. The gain drifts derived from the two xenon lamp systems were in reasonable agreement with each other.

Stability of ADC pedestals, high voltages, and temperature are all important. During the data-taking period, all the ADC pedestals were monitored every 12 h. All high voltages for photomultipliers were recorded for every beam spill throughout physics runs and checked in

off-line analysis. The temperatures of the experimental area and of several positions of important detector elements were continuously recorded.

IV. DATA TAKING

We took data under the following triggering conditions: (i) a slow antiproton was incident on the liquid-hydrogen cell, and (ii) one or two γ rays fell on the NaI. As shown in the electronics diagram, Fig. 10, an antiproton in the beam was first selected by the time of flight between S1 and S2. A large dE/dx signal in S4 was then required to verify that a slow antiproton was incident on the liquid-hydrogen cell. When this requirement was met, ADC, time-to-digital converter (TDC), and MWPC memory modules were immediately activated. In the subsequent 140 ns, a fast cluster-counting-logic (CCL) circuit²² counted the multiplicities of charged and neutral clusters separately and, if they satisfied the preselected criteria (one or two γ rays), generated a "yes" signal. A master trigger signal was then generated immediately to continue the data taking and to transfer the data into an on-line PDP-11/34A computer. Otherwise, the event was canceled by the fast clearing of the ADC, TDC, and MWPC memory modules.

In the CCL, charged particles in the barrel as well as the end-cap hodoscopes were counted to give the charge multiplicity. The multiplicity of neutral clusters in the NaI was given by subtracting the number of charged particles from the total number of clusters in the NaI. The former was simply obtained by counting hits in the barrel hodoscope in front of the NaI. To count the latter, the pulse height of each NaI module was first discriminated at 20 MeV to give "hit" or "no hit" patterns on the NaI. Then, for economy of time, the counting of hits was done one dimensionally after having taken an OR condition of six NaI modules on the same azimuthal positions (see Fig. 11). More complete and sophisticated two-dimensional reconstruction was done later in off-line analysis. In the CCL, for simplicity, odd charge multiplicities were translated into even ones by adding one. Various choices of the neutral- and charged-particle multiplicities were possible by the use

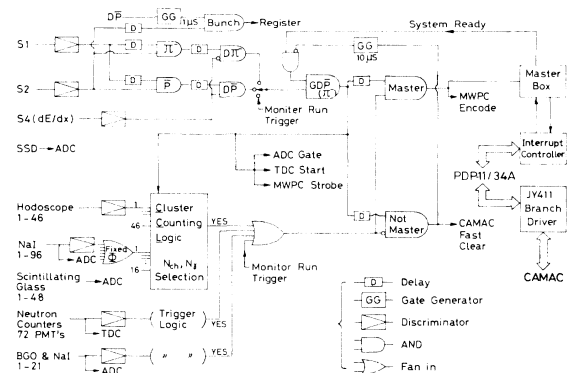


FIG. 10. A schematic electronics diagram.

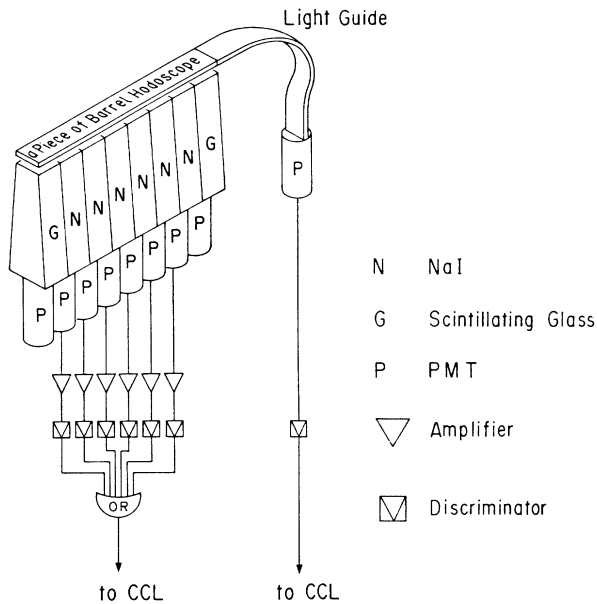


FIG. 11. Electronic connection of γ modules and barrel hodoscope to the CCL (see the text). Only an azimuthal 10 degree unit is sketched.

of selection switches. In the physics runs, data were taken for a neutral-particle multiplicity of 1 or 2 with any charge multiplicities. In the calibration runs with the stopping π^- beam, a charge multiplicity of zero was required.

On-line data acquisition was executed by RTMULTI (Ref. 23) with the interface JY411; see a schematic diagram presented in Fig. 12. Event data during each beam spill were buffered in the memory of the PDP-11 and written into a magnetic tape between beam spills.

In parallel with the data taking, a part of the data was constantly analyzed on line in order to check the performance of the whole detector. For example, the efficiency of each wire plane was monitored run by run. Distributions of hit anode wires and of hit cathode strips in each MWPC were also summarized in order to detect dead channels.

Since the stability of the γ detectors was essential, the following monitoring and calibration runs were periodically inserted between physics runs: (i) xenon lamp runs to monitor gain drifts, (ii) pedestal runs to monitor ADC pedestals, and (iii) stopping π^- runs for calibration (see Sec. III).

Besides the above physics runs and monitoring and calibration runs, the following check runs were also carried out: (i) empty-target runs to estimate the effect of target walls and of the vacuum container, (ii) runs with antiprotons stopping in the degrader, (iii) various non-selective trigger runs (no selection on the TOF or the dE/dx or the CCL) to estimate triggering biases and backgrounds, and (iv) 580-MeV/c π^- beam runs to check alignment of detectors along the beam.

In order to switch various types of runs as described above, two control circuits were prepared:²² an interrupt

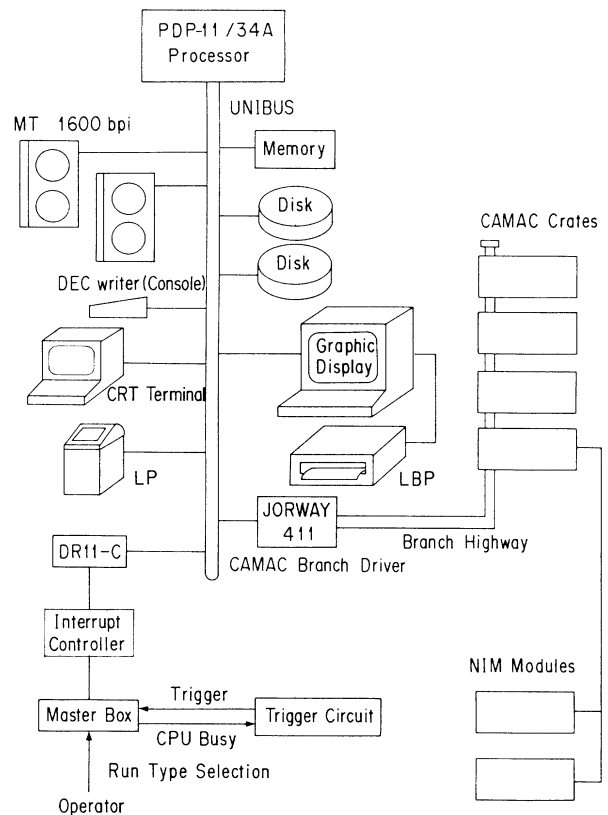


FIG. 12. A schematic drawing for the on-line data-acquisition system.

controller for the PDP-11 and master box for selecting run types. For example, when a xenon lamp run was selected, the master box opened the shutters for xenon lamps, suppressing interrupts from physics run triggers.

The number of TOF-selected antiprotons was typically 570 per beam burst. The slow antiprotons downstream of the degrader ($D\bar{P}$, see Fig. 10) were about 370 per burst, 55% of which occurred during the computer ready time. By requiring one or two γ rays in the NaI, about 90 events were finally triggered and written on magnetic tapes. If a slow antiproton ($D\bar{P}$) was accidentally accompanied by another beam particle, usually a pion, within 1 μ s, a bunch flag was raised in the CAMAC register (see Fig. 10). Such bunched beam events were rejected in off-line analysis.

Contamination of π^- in the TOF-selected antiprotons owing to a tail in the TOF spectrum should be negligibly small, as the difference of 19 ns in the TOF was many times the rms width (less than 1 ns) of the TOF (see Fig. 13). Antiprotons were actually selected with a coincidence circuit having the rise/fall time of 1.5 ns and a flat top of 8 ns. Contamination of π^- then arose mainly from accidental coincidence of two pions. From check runs with a 580-MeV/c π^- beam, the contamination of π^- was found to be as small as 8×10^{-3} per TOF-selected antiproton, which was the right order of magnitude expected from two pions entering the TOF counters by chance within the coincidence time. As the dE/dx

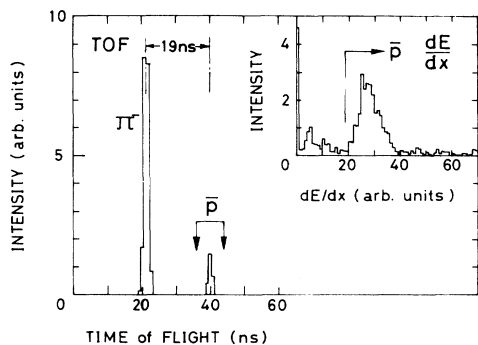


FIG. 13. A TOF spectrum between $S1$ and $S2$ obtained with a TDC. $S2$ was actually used for the start. The arrow shows the full width at half maximum (FWHM) (8 ns) of the coincidence. The dE/dx spectrum in $S4$ for the TOF-selected antiprotons is plotted in the inset. The arrow shows the discriminator cut for selecting slow antiprotons.

cut (see Fig. 13) gave an additional reduction factor of $\frac{1}{700}$, contamination of π^- in the slow antiprotons ($D\bar{P}$) was estimated to be less than 2×10^{-5} per $D\bar{P}$. It was further reduced in the off-line analysis by requiring only one beam particle and by requiring γ rays in the NaI. The π^- contamination can be, therefore, completely ignored in the search for discrete energy γ lines even with yields down to 10^{-4} .

In order to speed up the data acquisition, event data were compressed before transfer to JY411. When the γ modules and the cathode strips of the cylindrical MWPC's were read out by the LeCroy 2285A ADC's (with a 400-ns gate), only meaningful data were selected after pedestal subtraction by the control circuit (LeCroy 2280). The anode wire data of all the MWPC's were, after strobing in the KEK-type memory modules,²⁴ encoded and stored in the CAMAC memory buffer circuits.²⁵

V. DATA REDUCTION

A. Tracks and vertex reconstruction

From 3.6×10^7 triggered events in total, we first removed events (about 5.0%) which had hardware errors in the readout (too many words). We then removed spurious incident-beam events: (i) a beam-bunch flag was raised (1.7%), (ii) too many wires fired in the beam MWPC's [2.3% after rejection of (i)], or (iii) tracking failed. The total reduction factor for (i)–(iii) was 0.85. We then removed events in which tracking of the degraded antiprotons through $W6$ – $W7$ was unsuccessful: (i) no reconstructed track downstream of the degrader or (ii) multiple tracks with their crossing point ambiguous or far from the liquid-hydrogen cell. An additional reduction factor of 0.93 was mostly due to (i). From the above selections, about 75% of the events had a track of a slow antiproton directed toward the target.

For the accepted events, the vertex point was determined from the incoming slow antiproton and all the secondary charged particles. Figure 14(a) gives a distri-

bution of appropriately weighted rms distance from the vertex point to the tracks, calculated for events whose vertex could be reconstructed three dimensionally. As seen in this figure, the vertex was determined with the standard deviation (1σ) of 9 mm. In the radial and longitudinal distributions of the vertex points [see Figs. 14(b) and 14(c), respectively], the walls of the target and of the vacuum chamber are clearly seen. When none of the secondary tracks could be successfully reconstructed three dimensionally owing to small inefficiencies in the cathodes of MWPC's, or when the final state was entirely neutral, the SSD pulse height was employed to determine the longitudinal vertex position. The antiproton range versus SSD pulse height was calibrated for those

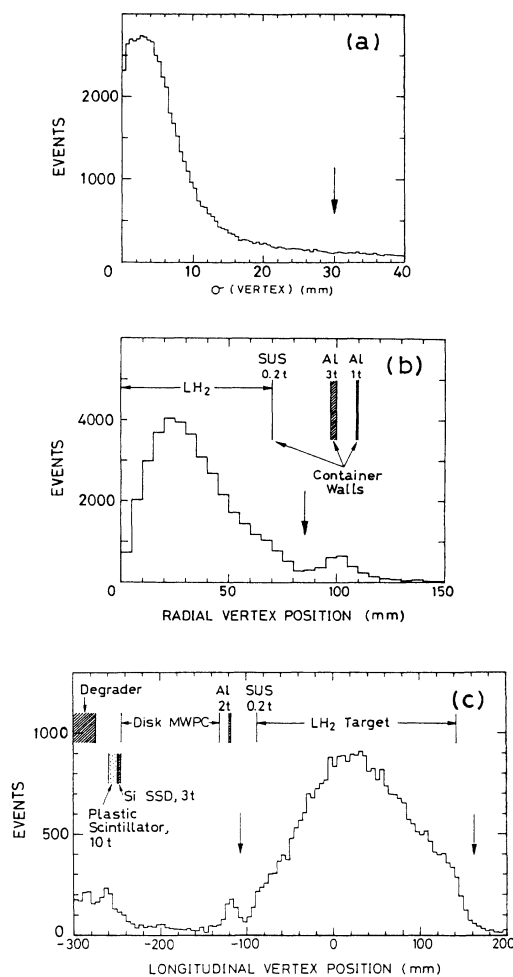


FIG. 14. Vertex distribution in a typical stopping antiproton run. Arrows show the cut positions for data reduction. (a) Distribution of the rms distance from the vertex to the tracks in events whose vertex could be determined three dimensionally. (b) [or (c)] Distribution of radial [or longitudinal] vertex position for the events whose longitudinal [or radial] position fell in the liquid-hydrogen cell by more than 1 cm deep from the walls with the σ (vertex) less than 3 cm [or 1 cm]. The origin of the longitudinal coordinate ($z=0$) is set at the center of the NaI calorimeter.

events whose vertex points could be determined from charged tracks (see Fig. 15). Reconstruction of the vertex point was successful for 67% of the above accepted events after the following vertex cuts: (i) the rms derivation between the vertex and the charged tracks should be less than 3 cm and (ii) the vertex should not lie outside the target cell more than 2 cm longitudinally and 1.5 cm radially. We obtained finally 1.78×10^7 events after the above vertex cuts.

Events with odd charge multiplicities occurred due to two reasons: (i) track-reconstruction efficiency was less than unity because of acceptance gaps and of small inefficiencies of wire planes and (ii) γ rays from π^0 decay were conserved into e^+e^- pairs (about 6% per γ ray) in the target cell as well as in the vacuum chamber walls. Abundance of various prong events after reconstruction was as follows: 4.1% for 0, 6.0% for 1, 31.9% for 2, 21.8% for 3, 25.8% for 4, 7.2% for 5, and 2.6% for 6 prong events. As all neutral events are small, singly charged events must dominantly come from doubly charged ones. The effective efficiency of track reconstruction for secondary charged particles was then estimated to be about 90% from the abundance ratio of singly to doubly charged events. This value seems reasonable when it is compared with the purely geometrical one of 93% based on the acceptance gaps.

B. γ rays

γ rays were identified by energy deposits in the NaI and lack of signals in the scintillator hodoscope and in the MWPC in front of the hit NaI modules. Usually, each γ ray or, less frequently, each charged particle deposits energies in a cluster of modules. Sometimes, two clusters partially overlap each other because the average multiplicity of charged particles and γ rays is as large as

several per $\bar{p}p$ annihilation. Consequently, a cluster logic was applied in the data analysis to isolate each γ ray from neighboring charged particles or γ rays. Clusters were found by searching for peaks in the two-dimensional energy distribution on the NaI. Each module was first assigned to be either "hit" or "not hit," depending on whether or not the energy deposit exceeded a threshold of 0.7 MeV, which corresponded roughly to twice the fluctuation (1–2 channels) of ADC pedestals. By the above classification, the hit modules were grouped into connected regions. Peaks were then searched for in the energy deposit distribution within each connected region. When only one peak existed in the region, this region was taken as a cluster itself. Two peaks were taken as two clusters if the peaks were separated from each other by at least one module whose pulse height was less than the peaks by more than 5%. More than two peaks can be treated in a similar way. When a connected region was divided into two clusters, some of the modules should be shared by both the clusters. Instead of being shared, each module was simply connected to one of the neighboring modules having the largest energy deposit, and was cut off from the other modules. Neutral clusters consisting of only one hit module were rejected as they were most probably neutrons or very low-energy γ rays. For the obtained γ rays, we further required that the shower leakage into the scintillating glass be less than 10% of the γ -ray energy and finally obtained 1.64×10^7 γ rays above 10 MeV.

VI. ANALYSIS AND RESULT

A. Narrow peaks in γ -ray spectra

Inclusive γ -ray spectra are presented in Fig. 16 for the sum over the charge multiplicity, N_{ch} , as well as for each charge multiplicity separately. The number of γ rays in each spectrum is 0.85×10^6 for $N_{ch}=0$, 7.14×10^6 for $N_{ch}=2$ (actually the sum of multiplicities 1 and 2), 7.15×10^6 for $N_{ch}=4$ (3 and 4) and 1.17×10^6 for $N_{ch} \geq 6$ (larger than 4).

Each spectrum was fitted with a polynomial background plus narrow peaks by using the minimization program MINUIT (Ref. 26). In order to reduce the number of variables and thereby to improve stability in fitting, we have divided the whole energy range (80–980 MeV) into four parts with ample overlaps between adjacent regions. The order of polynomial between 2 and 4, mostly 3, was sufficient for obtaining good fits. Narrow peaks were expressed by asymmetric Gaussians: the ratio of the left to right side widths of the Gaussians, σ_L/σ_R , was varied from 2.1 at 100 MeV to 1.1 at 1000 MeV according to the result of an electron beam test with the 5×5 array of NaI modules. In order to search for peaks with intrinsic widths much smaller than the instrumental one, the widths of the peaks were fixed within $\pm 20\%$ above the instrumental one. The fitted results, after subtraction of the polynomial background, are presented in Fig. 17 for the sum over the charge multiplicity, and in Fig. 18 for each charge multiplicity separately. In Fig. 17, the peaks observed by Richter

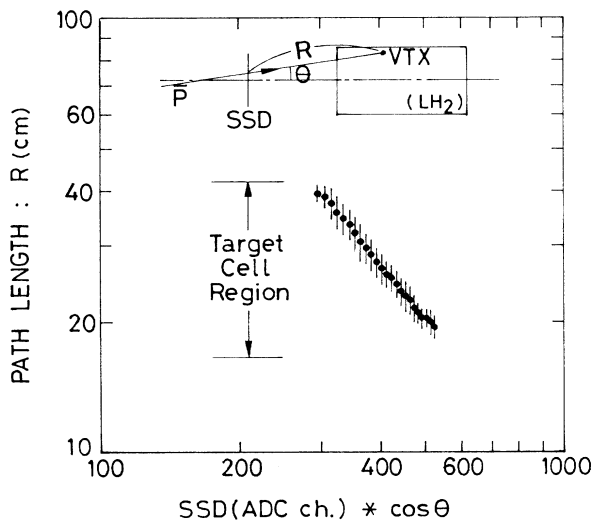


FIG. 15. Antiproton range vs SSD pulse height obtained in a typical stopping antiproton run for events whose vertices were successfully determined three dimensionally from charged tracks with an ambiguity (1σ) less than 3 cm. Bars on the data points show the measurement error (1σ).

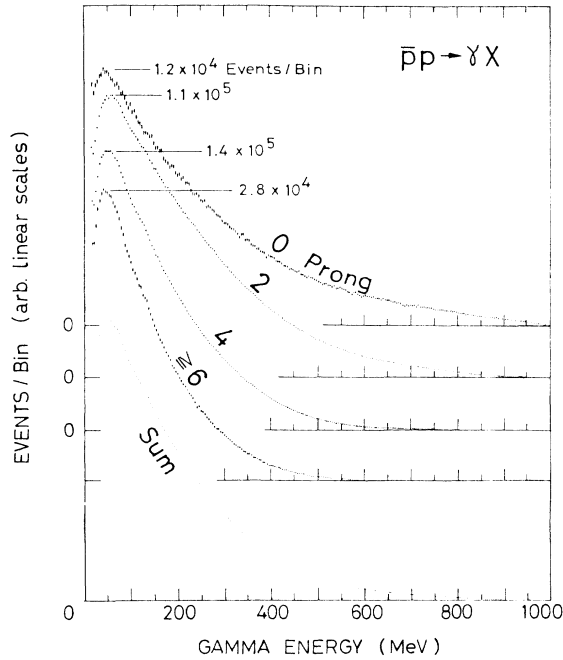


FIG. 16. Inclusive γ -ray spectra for various charge multiplicities as well as for their sum. Events with odd multiplicities of 1, 3, and 5 were added to those with even multiplicities of 2, 4, and 6, respectively. Bars on the data points show statistical errors (1σ). Number of events per 4.16-MeV bin is given at the peak of each spectrum.

*et al.*⁵ are also plotted with dashed curves with the instrumental resolution of the present detector folded in.

B. Yields of peaks

Yields of $\bar{p}p \rightarrow \gamma B$ can be calculated from the area of the narrow peak in the inclusive γ -ray spectra. The yield per $\bar{p}p$ annihilation Y is, by definition, given by the number of monochromatic γ rays (peak area A) divided

by the number of annihilations corrected for the detection efficiency:

$$N_{\bar{p}} Y \eta_B(E) = A. \quad (3)$$

Here $N_{\bar{p}}$ is the number of annihilations and $\eta_B(E)$ is the detection efficiency of γ rays with energy E including hardware and software cuts. As $N_{\bar{p}}$ is proportional to N_γ , the total number of γ rays in the inclusive γ -ray spectrum (1.64×10^7), we obtain another relation:

$$N_{\bar{p}} \int \rho(E') \eta(E') dE' = N_\gamma, \quad (4)$$

where $\rho(E') dE'$ is the number of γ rays (mostly coming from π^0 decay) with energies between E' and $E' + dE'$ per annihilation. The detection efficiency of γ rays, η , may be different from η_B because the final state of γB is different from that of $\bar{p}p$ annihilation. Substitution of Eq. (4) into Eq. (3) gives

$$Y = K(E) A / N_\gamma, \quad (5)$$

where

$$K(E) = \int \rho(E') \eta(E') dE' / \eta_B(E) \quad (6)$$

is the effective multiplicity of γ rays per annihilation. Equation (5) with $K(E)$ given by Eq. (6) is simpler than Eq. (3) because some factors, such as the geometrical acceptance of the NaI, the shower leakage into the scintillating glass, etc., are canceled in the numerator and denominator of $K(E)$. We have calculated yields according to Eqs. (5) and (6) with $K=4.45$ (see Appendix A [Eq. (A1)]). The obtained yields are presented in Table I for peaks with statistical significance higher than 1.9σ .

The most prominent peak was due to the Panofsky γ rays at 129 MeV. Its yield of $(4.52 \pm 0.36) \times 10^{-3}$ per annihilation is consistent with an estimation (5.25×10^{-3}) derived from the following numbers: the π^- multiplicity per $\bar{p}p$ annihilation = 1.53 (Refs. 27 and 28), and Panofsky ratio = 1.546 ± 0.009 (Ref. 29), and the average prob-

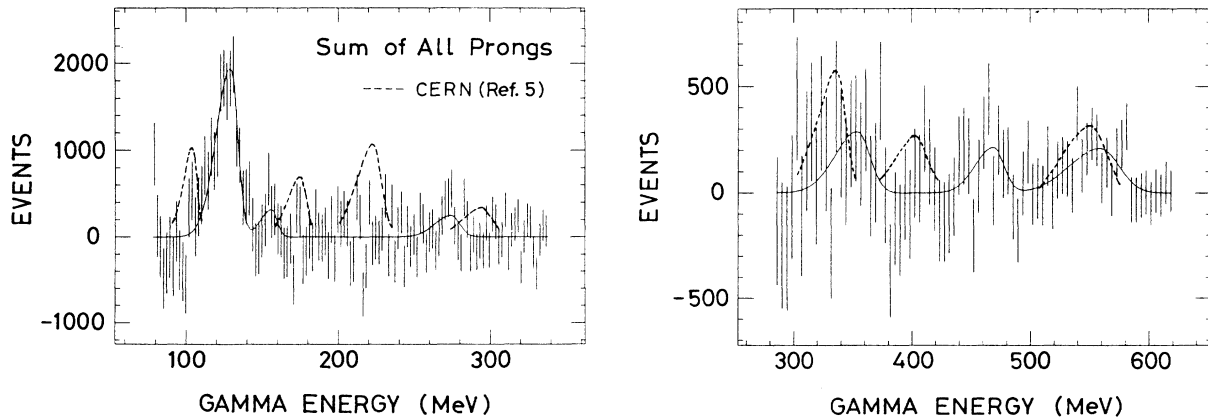


FIG. 17. A fit to the inclusive γ -ray spectrum from $\bar{p}p$ annihilation at rest with a polynomial background plus narrow asymmetric Gaussians. The residue after subtraction of the background is presented. The bin width is 2.08 MeV for the figure on the left and twice that width on the right. For the dashed curves, see the text.

ability that a π^- meson stops in the liquid hydrogen = 0.87% corresponding to the pion range of 7 cm. The last number was deduced from the π^- momentum distribution, which was calculated in a Monte Carlo simulation for $\bar{p}p$ annihilation by including the channels and branching ratios listed in Table II (see Appendix B).

Except for the Panofsky γ -ray peak, we have seen nine narrow peaks at $E_\gamma = 140, 156, 227, 275, 320, 356, 423, 468,$ and 560 MeV with a statistical significance at 2 to 3σ levels. The yields of these peaks are also plotted, in Fig. 19, in comparison with the result of Richter *et al.*⁵ The solid curves in Fig. 19 give the yields which

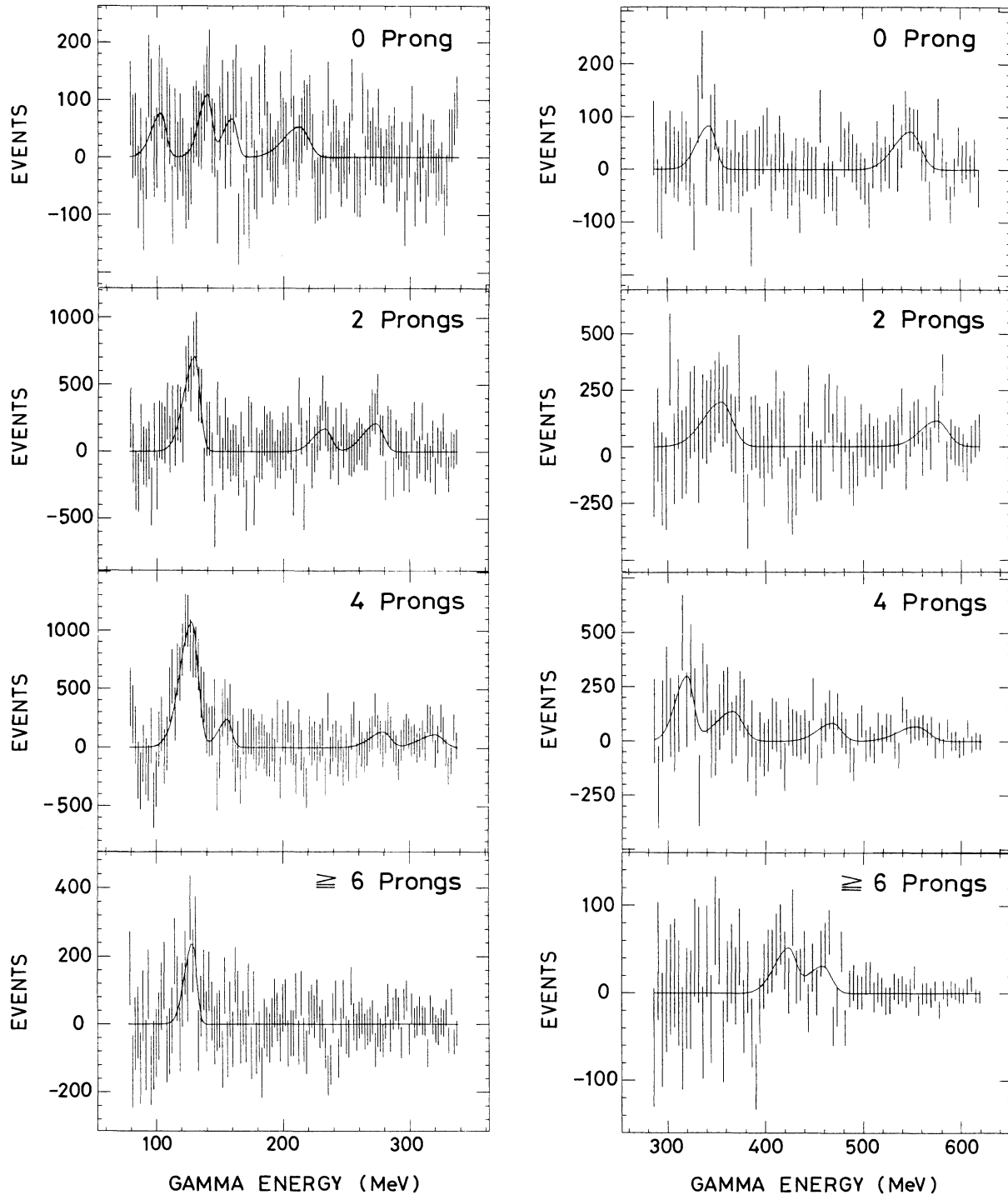


FIG. 18. A fit to the inclusive γ -ray spectrum for each charge multiplicity. The other items are the same as for Fig. 17.

TABLE I. Experimental result on narrow states. Position, yield per annihilation, statistical significance, and width are given for each peak in γ -ray spectra. The width was made variable within the instrumental width $\pm 20\%$: (U) and (L) denote the upper and lower limits, respectively. For the case of U (or L), the error of width is meaningful only with the minus (or plus) sign, and is given in parentheses. The column of notes gives the weight-averaged position of the γ -ray peak. The mass of B for the reaction of $\bar{p}p \rightarrow \gamma B$ is also given in parentheses.

	Charge multiplicity (N_{ch})					Notes
	$N_{\text{ch}} = \text{all}$	0	2	4	≥ 6	
Position (MeV)	129.2 \pm 0.7		129.8 \pm 1.0	128.1 \pm 0.9	128.8 \pm 1.1	129.0 \pm 0.8
Yield (10^{-3})	4.52 \pm 0.36		1.45 \pm 0.33	2.48 \pm 0.25	0.37 \pm 0.08	Panofsky γ
Statistical significance	12.4 σ		4.4 σ	9.8 σ	4.7 σ	
Width σ (MeV)	6.8(0.2, U)		6.0 \pm 1.8	6.8(0.2, U)	4.5(2.1, L)	
Position (MeV)		139.9 \pm 1.4				139.9 \pm 1.4
Yield (10^{-3})		0.18 \pm 0.06				(mass M_B in MeV/ c^2 = 1731.0 \pm 1.5)
Statistical significance		2.9 σ				
Width σ (MeV)		4.8(1.7, L)				
Position (MeV)	156.1 \pm 2.6	159.3 \pm 2.0		155.8 \pm 2.2		156.4 \pm 2.4
Yield (10^{-3})	0.56 \pm 0.29	0.13 \pm 0.06		0.42 \pm 0.20		(1713.0 \pm 2.6)
Statistical significance	1.9 σ	2.0 σ		2.1 σ		
Width σ (MeV)	5.2(2.4, L)	5.3(2.1, L)		5.2(2.4, L)		
Position (MeV)		212.9 \pm 4.0	232.9 \pm 3.4			227.2 \pm 3.6
Yield (10^{-3})		0.16 \pm 0.08	0.40 \pm 0.19			(1633.6 \pm 4.1)
Statistical significance		2.0 σ	2.1 σ			
Width σ (MeV)		9.4(3.1, U)	7.0(2.8, L)			
Position (MeV)	274.2 \pm 3.0		273.4 \pm 2.3	279.2 \pm 3.5		275.0 \pm 2.9
Yield (10^{-3})	0.66 \pm 0.29		0.56 \pm 0.21	0.36 \pm 0.19		(1577.8 \pm 3.4)
Statistical significance	2.3 σ		2.6 σ	1.9 σ		
Width σ (MeV)	7.9(2.7, L)		7.8(2.7, L)	8.0(3.9, L)		
Position (MeV)				319.6 \pm 2.9		319.6 \pm 2.9
Yield (10^{-3})				0.44 \pm 0.13		(1523.8 \pm 3.6)
Statistical significance				3.3 σ		
Width σ (MeV)				8.8(4.0, L)		
Position (MeV)	353.9 \pm 7.9	342.5 \pm 3.9	355.6 \pm 6.9	366.4 \pm 6.6		355.9 \pm 7.0
Yield (10^{-3})	0.69 \pm 0.31	0.13 \pm 0.06	0.48 \pm 0.24	0.31 \pm 0.14		(1478.4 \pm 8.9)
Statistical significance	2.2 σ	2.0 σ	2.0 σ	2.3 σ		
Width σ (MeV)	14.2(3.9, U)	9.3(3.9, L)	14.3(3.5, U)	13.6 \pm 3.4		
Position (MeV)					422.8 \pm 4.7	422.8 \pm 4.7
Yield (10^{-3})					0.09 \pm 0.04	(1390.9 \pm 6.3)
Statistical significance					2.6 σ	
Width σ (MeV)					10.8(5.0, L)	
Position (MeV)	468.7 \pm 5.4			467.9 \pm 5.8	458.3 \pm 3.9	467.5 \pm 5.4
Yield (10^{-3})	0.42 \pm 0.19			0.17 \pm 0.08	0.06 \pm 0.03	(1329.2 \pm 7.6)
Statistical significance	2.2 σ			2.1 σ	2.0 σ	
Width σ (MeV)	11.7(5.3, L)			11.7(5.6, L)	11.5(3.9, L)	
Position (MeV)	559.0 \pm 7.3	548.8 \pm 3.7	575.4 \pm 5.0	553.6 \pm 5.9		560.3 \pm 6.3
Yield (10^{-3})	0.71 \pm 0.28	0.16 \pm 0.06	0.26 \pm 0.13	0.17 \pm 0.06		(1191.0 \pm 9.9)
Statistical significance	2.5 σ	2.8 σ	2.1 σ	3.1 σ		
Width σ (MeV)	20.0(5.1, U)	13.1(4.4, L)	13.6(6.2, L)	14.9 \pm 5.8		

correspond to four times the statistical fluctuation of the background γ rays, which fall into an energy span of \pm instrumental FWHM.

Though a few more peaks have been observed above 600 MeV in the inclusive γ -ray spectra, they could be assigned to monochromatic π^0 peaks coming from $\bar{p}p \rightarrow \pi^0 M$ with $M = \pi^0/\gamma, \eta, \rho^0/\omega$, etc., and they are removed from both Fig. 19 and Table I. Misidentification of π^0 as a single γ ray occurred at higher energies because spatial separation between the two decay γ rays was incomplete within the granularity of the present calorimeter. The probability of such misidentification increased with the γ energy but remained negligibly small (less than a few percent) at π^0 (total) energies below 500 MeV (see Appendix A). The 560-MeV peak, the highest-energy one below 600 MeV, must not be due to monochromatic π^0 . Should this peak be due to monochromatic π^0 , its yield should be much larger than 1% according to a Monte Carlo calculation (see Appendix A). Actually, the fact that no such large peak was observed in the inclusive π^0 spectrum³⁰ excludes the possibility that the above peak might be due to π^0 mesons.

None of the observed peaks could be assigned to minimum-ionizing particles, which deposited about 185 MeV in the NaI (see Appendix C), because contamination of charged particles was negligibly small (see Appendix C).

We have not observed any statistically significant γ -ray peaks around 103 MeV, where a 3 to 4σ peak with yields larger than 10^{-3} was reported in previous experiments.^{5,6} As the 103-MeV peak should sit in the valley between the “box spectrum” between 55 and 83 MeV ($\pi^-p \rightarrow \pi^0 n \rightarrow \gamma\gamma n$) and the monochromatic γ -ray peak at 129 MeV ($\pi^-p \rightarrow \gamma n$), the conclusion about this peak may depend on the shape of the $\pi^-p \rightarrow \gamma n, \gamma\gamma n$ spectrum. To check this point, we have reanalyzed the range of 50–200 MeV by employing a high-statistics experimental spectrum instead of a Gaussian approximation for the Panofsky γ rays. The γ -ray spectrum was fitted with the sum of a polynomial background of order 3–4, the experimental γ -ray spectrum from $\pi^-p \rightarrow \gamma n, \gamma\gamma n$ (only its intensity being variable) and narrow asymmetric Gaussians. The fitted result is presented in Figs. 20 and 21 after subtraction of the

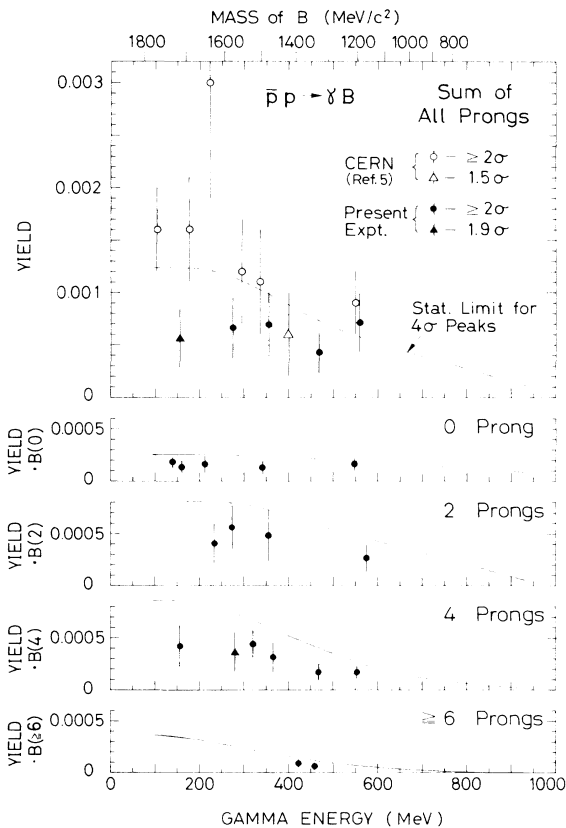


FIG. 19. Yields of the narrow peaks, seen in the inclusive γ -ray spectra from $\bar{p}p$ annihilation at rest, are plotted with solid circles (for peaks with statistical significance higher than 2σ) and solid triangles (1.9σ). The CERN data (Ref. 5) are also shown for comparison with open circles (higher than 2σ) and open triangles (1.5σ). The Panofsky γ rays at 129 MeV are not shown. For the solid curves, see the text.

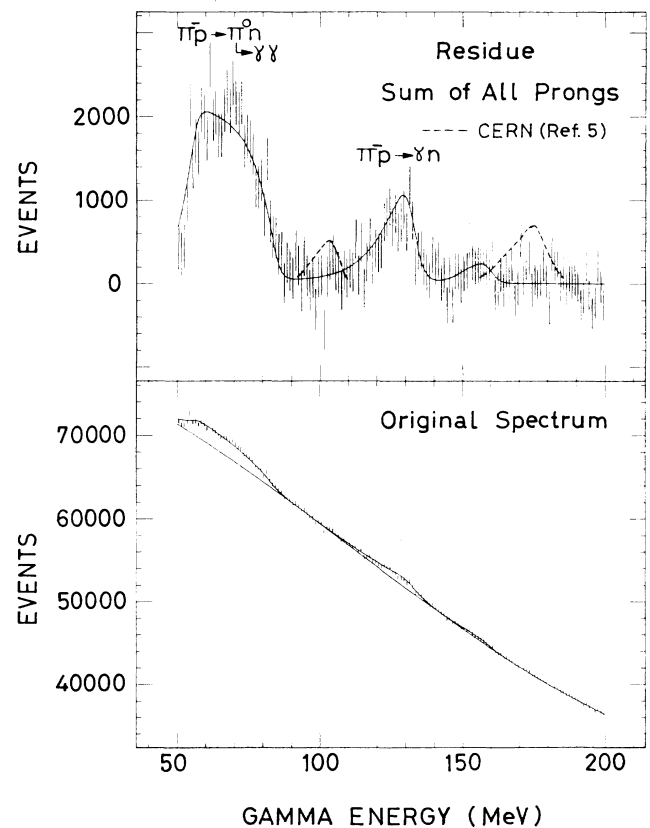


FIG. 20. A fit to the inclusive γ -ray spectrum summed over the charge multiplicity in the energy range of 50–200 MeV: original spectrum on the bottom and the residue after subtraction of the polynomial background on the top. An experimental spectrum for $\pi^-p \rightarrow \gamma n, \gamma\gamma n$ was used. For the dashed curves, see the text.

background. In the spectrum summed over the charge multiplicity (see Fig. 20), the dashed curve shows Gaussian peaks which should arise if the narrow states in Ref. 5 should really exist. These peaks are plotted with the instrumental resolution of the present detector folded in.

No statistically significant peak was observed around 103 MeV: the 4σ upper limit is 1.2×10^{-3} . Among the spectra with various charge multiplicities (see Fig. 21), the spectrum for zero prong events gave the largest peak around 103 MeV with a yield of 0.14×10^{-3} at a statisti-

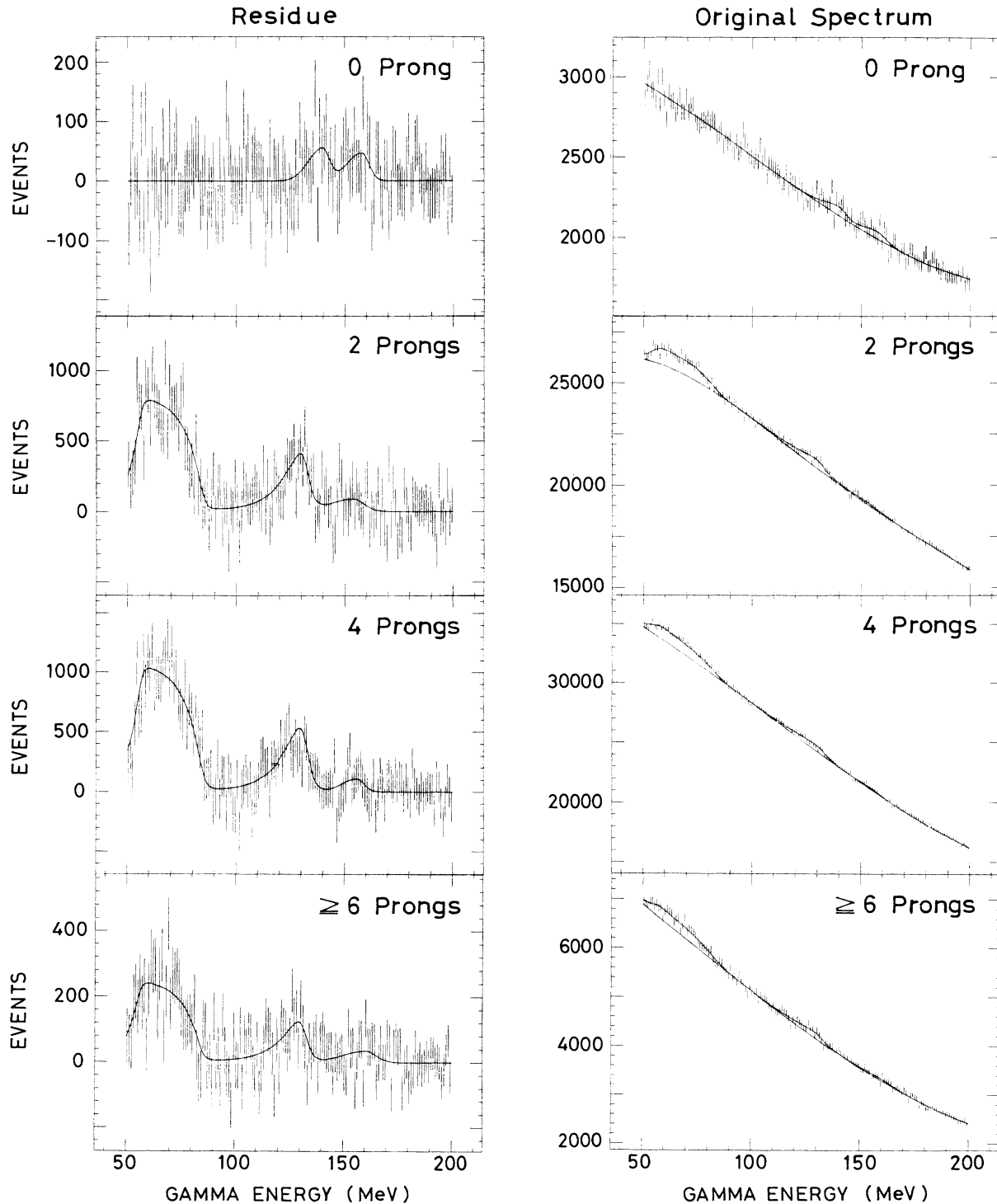


FIG. 21. A fit to the inclusive γ -ray spectrum in the energy range of 50–200 MeV for the charge multiplicities of 0, 2, 4, and ≥ 6 , separately. Original spectra are shown on the right side and the residue on the left. The other items are the same as for Fig. 20.

cal significance of 1.4σ . This result was the same as in the analysis with the Panofsky peak approximated by an asymmetric Gaussian.

When the size of the energy range, the order of polynomial for the background, the number of narrow peaks, etc., were varied, the fitted result for the background varied slightly. As the background was very large, a slight change in the background sometimes caused a sizable change in the peak areas. The overall systematic error for the yields of individual narrow states was estimated to be less than 50% from comparison between different fitting conditions as described above. Other items such as different binnings, different vertex cuts, slightly different sets of calibration coefficients for γ modules, etc., did not much affect the result.

Owing to the triggering condition of one or two γ rays on the NaI, the detection efficiency for $\bar{p}p \rightarrow \gamma B$ decreases as the γ -ray multiplicity in the decay of B increases. Comparing $K(E)$ of Eq. (6) for various simple decay channels of B in a Monte Carlo calculation (see Appendix A), we find that the obtained yield may vary within $\pm 20\%$ depending on which specific channels should be preferred in the decay of B . $K=4.45$, which falls on the higher side within the possible range, has been used for safety in estimating the upper limits for baryonium production.

VII. DISCUSSION ON THE OBSERVED NARROW STATES

Here we list a few facts which may help determine whether or not the observed peaks are real. The following indicate that the observed peaks may be real.

(i) Six peaks at 156, 227, 275, 356, 468, and 560 MeV have been simultaneously seen in the spectra with more than one different charge multiplicity.

(ii) The energy range of 80–600 MeV includes 22 independent bins in units of the instrumental FWHM. The probability that N peaks of 2σ significance are created by statistical fluctuation is as small as 19% for $N=2$, 6% for 3, and 1.4% for 4.

(iii) When we divided the entire data into the earlier and later halves with respect to the data-taking period, the two spectra gave essentially the same result, as shown in Fig. 22.

(iv) Yields of the Panofsky peak at 129 MeV for different charge multiplicities are consistent with qualitative expectation: zero for 0 prong, large for both 2 and 4 prongs, and small for ≥ 6 prongs. Again their sum is compatible with the rate obtained from the inclusive γ -ray spectrum for the sum of all prongs.

The following indicates that the observed peaks may not be real.

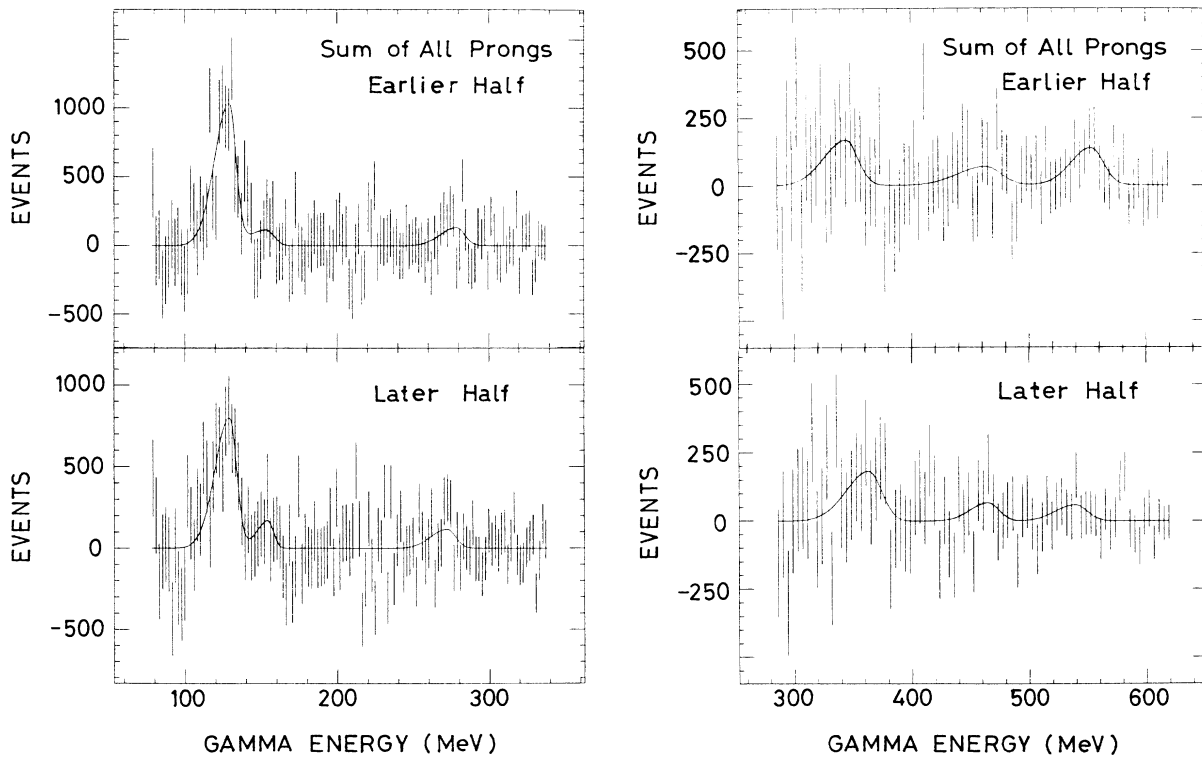


FIG. 22. Comparison between two inclusive γ -ray spectra, after subtraction of the polynomial background, obtained in the earlier (the top: 50% of all data)-and later (bottom: 43%) halves of the data-taking period.

(i) The yield of each peak is as small as the sensitivity of the experiment for 2 to 3σ peaks. Experience^{5,6} tells that controversial results may sometimes appear for peaks with a statistical significance as small as 2σ .

VIII. SUMMARY AND DISCUSSION

The above results are summarized as follows.

(1) By fitting the inclusive γ -ray spectra from $\bar{p}p$ annihilation at rest with a polynomial background plus narrow Gaussians, we have not observed, besides the Panofsky γ rays at 129 MeV, any narrow peaks with statistical significance higher than 4σ . The 4σ upper limit for the yield of $\bar{p}p \rightarrow \gamma B$ per annihilation times $B(N_{\text{ch}})$, where $B(N_{\text{ch}})$ is the decay branching ratio of B into N_{ch} -prong states, is $(1.2-0.2) \times 10^{-3}$ at the γ energy $E = 80-938$ MeV for the sum over N_{ch} , $(0.3-0.1) \times 10^{-3}$ for each of $N_{\text{ch}}=0$ and ≥ 6 , and $(0.8-0.1) \times 10^{-3}$ for each of $N_{\text{ch}}=2$ and 4.

(2) At 2 to 3σ levels, we have seen nine narrow peaks at E (in MeV) = 140 ($M_B = \text{mass of } B$ in $\text{MeV}/c^2 = 1731$), 156 ($M_B = 1713$), 227 ($M_B = 1634$), 275 ($M_B = 1578$), 320 ($M_B = 1524$), 356 ($M_B = 1478$), 423 ($M_B = 1391$), 468 ($M_B = 1329$), and 560 ($M_B = 1191$). These peaks have yields between 10^{-4} and 10^{-3} per annihilation.

(3) The arguments for the notion that the observed peaks are real are the simultaneous occurrence of the same peaks in the spectra with different charge multiplicities, consistency between the two data sets in the earlier and later halves of the data-taking period with respect to the existence of the narrow peaks, and the successful and consistent fitting result for the Panofsky γ rays. The arguments against are their small yields close to the sensitivity of the experiment for the statistical significance of only the 2 to 3σ level.

Recently, the results of two new experiments at LEAR have been reported. Adiels *et al.*³¹ have not confirmed their previous result⁵ and have given the 4σ upper limit for baryonium production of $(0.2-1.0) \times 10^{-3}$ for M_B between 1040 and 1770 MeV/c^2 from 2.4×10^7 γ rays measured with bismuth germanate (BGO) detectors. A characteristic feature of their analysis is the subtraction of a continuous background spectrum that was obtained by approximating a Monte Carlo simulation of the spectrum with a smooth function. Angelopoulos *et al.*³² have given the 4σ upper limit of $(0.5-1.3) \times 10^{-3}$ for M_B between 940 and 1700 MeV/c^2 [$(1.3-2.5) \times 10^{-3}$ for M_B between 1700 and 1800 MeV/c^2]. They used a magnetic e^+e^- pair spectrometer to measure γ rays and obtained 4.8×10^6 γ rays with the energy resolution better than that in the present experiment by a factor of 1.5–3 depending on the γ energy. Both results are similar to ours with respect to the upper limit of baryonium production, which is summed over the decay charge multiplicity.

The yields of narrow states seen in the present experiment have just reached the order of magnitude that is expected⁷ for baryonia consisting of a diquark-antidiquark pair in a quark potential model. Higher-statistics measurements in the future are important. The

rejection of γ rays from π^0 decay by exclusive measurement of all γ rays can considerably reduce the background, and will be a good direction for future pursuits.

A final remark goes to $\zeta(1480)$ (mass = 1477 MeV/c^2 , $\Gamma = 116 \text{ MeV}/c^2$) (Ref. 33), which have been observed in $\bar{p}n \rightarrow 3\pi^+ 2\pi^-$ and assigned to $I^G(J^{PC}) = 0^+(2^{++})$. The 356-MeV γ -ray peak observed in the present experiment satisfies the kinematics for $\bar{p}p \rightarrow \gamma \zeta(1480)$ (see Table I), but the statistical significance of this peak is insufficient to make further definite statements.

ACKNOWLEDGMENTS

The authors would like to express their gratitude to all the people who made the present experiment successful. Among them, the authors are especially thankful to Professor T. Nishikawa, Professor S. Ozaki, Professor H. Sugawara, and Professor H. Hirabayashi for their interest, support, and encouragement. Mr. H. Kaneko was very helpful in constructing and testing MWPC's. The authors are deeply indebted to the people of the proton synchrotron, and electronics group, the refrigerator facility group, the KEK workshop, and the computer center for helpful discussions and direct contributions, without which the present experiment could not have been achieved.

APPENDIX A: YIELD CALCULATION

The yield of a narrow peak in the inclusive γ -ray spectrum is given by Eq. (5) with $K(E)$ of Eq. (6). When the hardware event selection as well as software cuts are independent of γ -ray energy E , and there are no triggering biases, we can set $\eta_B(E) = \eta(E) = \text{const}$. In this approximation, K becomes equal to 3.93 (Ref. 34), the mean multiplicity of γ rays per annihilation.

As shown later, a Monte Carlo calculation for the present experiment shows that $\eta(E)$ is approximately independent of energy in the range (below 600 MeV) where $\rho(E)$ is large. As there is no reliable information about the decay scheme of B , we have assumed that the decay branching ratios of B into various channels are the same as in $\bar{p}p$ annihilation. As $\eta_B(E)$ is also approximately independent of energy in the above energy region, we obtain

$$K = 3.93 \eta / \eta_B . \quad (\text{A1})$$

The difference between η and η_B comes mainly from the trigger selection condition of one or two γ rays on the NaI. Estimating the ratio η/η_B in a simple approximation where γ rays are emitted independently and uniformly, we have

$$K = A_\gamma (\eta_1 + 2\eta_2) / (\eta_0 + \eta_1) = 4.45 , \quad (\text{A2})$$

where η_m is the probability that m γ 's among the average 3.93 γ 's fall on the NaI.

Besides the above simplified estimation, we have also estimated $K(E)$ by a Monte Carlo calculation for both $\eta(E)$ and $\eta_B(E)$. The energy dependence of $\eta(E)$ was calculated by generating events according to the annihi-

lation channels and branching ratios listed in Table II, by selecting events according to the actual triggering condition, and by applying to them the cluster logic and other software cuts. More details are described in Appendix B. The detection efficiency was found to be constant within $\pm 8\%$ below 600 MeV (see the solid curve in Fig. 23). Above 600 MeV, the detection efficiency increases with the energy, reaching a 40% increase at 900 MeV. This increase is due to a reduction in the amount of γ rays that are removed owing to their overlap with other particles; qualitatively, high-energy γ rays are associated with the low multiplicity of secondary particles. As the fraction of γ rays above 600 MeV is small, the above energy dependence causes only a small change in the integral $\int \rho(E')\eta(E')dE'$. The energy dependence of $\eta_B(E)$ was calculated in a similar Monte Carlo simulation for $\bar{p}p \rightarrow \gamma B$ and is shown with the chained curve in Fig. 23. It was found that $\eta_B(E)$ is nearly independent of energy below 400 MeV and increases as the energy increases beyond 400 MeV. The energy dependence of $\eta_B(E)$ is of a similar shape to and a little larger than that of $\eta(E)$. At low energies, $\eta_B(E)$ is smaller than $\eta(E)$. This is because the loss of γ rays, due to their overlap with other particles, is larger in $\bar{p}p \rightarrow \gamma B$ than in $\bar{p}p$ annihilation under the assumption that the particle multiplicity in the former is larger, by one, than in the latter. At high energies, on the contrary, $\eta_B(E)$ is larger than $\eta(E)$. This may be interpreted as follows: in ordinary $\bar{p}p$ annihilation, a high-energy γ ray mostly originates from a high-energy π^0 and tends to be lost by an overlap with its partner γ ray from the same π^0 owing to small opening angle between the two γ rays. The resultant $K(E)$, plotted in Fig. 24, is constant within $\pm 15\%$ below 600 MeV. Baryonia may, however, decay into final states having smaller particle multiplicities than in $\bar{p}p$ annihilation. Consequently, $K(E)$ for a few simple decay channels of B are also compared in Fig. 24. As the particle multiplicity decreases, η_B generally increases and K decreases. K has a value roughly between 3 and 5. As both the precise values and the energy dependence of K depend on the decay scheme of baryonia, which is not well known, we have adopted, for simplicity, the energy-independent value of K given by Eq. (A2).

When we calculate the yields according to Eq. (5), it is important that N_γ should not include particles other than γ rays. Contamination of charged particles was negligibly small as described in Appendix C. Employing a Monte Carlo simulation similar to that mentioned above, we have also estimated the probability of registering two γ rays from π^0 decay as single γ rays, owing to incomplete separation between the two γ rays. Such probability is negligibly small (less than a few percent) at π^0 total energies below 500 MeV; this probability slowly increases with the increasing energy and reaches 40% at 900 MeV. Considering a small yield of π^0 above 500 MeV (as small as 30% of the total π^0), the limited geometrical acceptance of the NaI for π^0 above 500 MeV (10–15%), and the above misidentification probability, we have concluded that contamination of π^0 increases the total number of γ rays (N_γ) by only less than 3%.

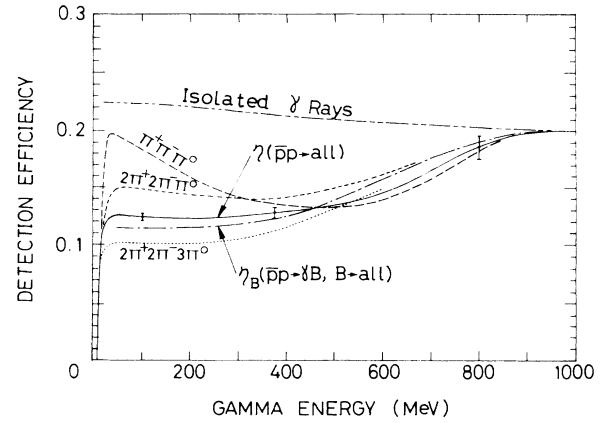


FIG. 23. Energy dependence of the γ -ray detection efficiency $\eta(E)$, which was obtained in a Monte Carlo calculation (see the text) for a few typical $\bar{p}p$ annihilation channels. The η for $\bar{p}p \rightarrow \pi^+\pi^-2\pi^0$ is similar to that for $2\pi^+2\pi^-\pi^0$. The η for both $\pi^+\pi^-3\pi^0$ and $2\pi^+2\pi^-2\pi^0$ are similar to $\bar{p}p \rightarrow \text{all}$, which denotes summation over the annihilation channels listed in Table II. Typical statistical errors of Monte Carlo simulation are also given. The η_B gives the detection efficiency of γ rays produced in $\bar{p}p \rightarrow \gamma B$. $B \rightarrow \text{all}$ means that decay channels and branching ratios of B are taken the same as for $\bar{p}p \rightarrow \text{all}$. Isolated γ rays show a hypothetical case where only a γ ray should be generated in the target without any accompanying particles.

APPENDIX B: MONTE CARLO SIMULATION OF $\bar{p}p$ ANNIHILATION, ETC.

The detection efficiencies $\eta(E)$ and $\eta_B(E)$ were calculated in a Monte Carlo method with the GEANT pro-

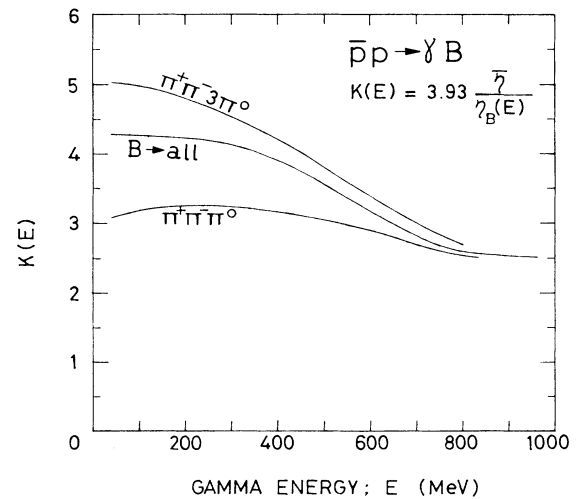


FIG. 24. The coefficient $K(E)$ in Eqs. (5) and (6), calculated by a Monte Carlo simulation. $B \rightarrow \text{all}$ shows that B is assumed to decay in the same channels and branching ratios as in $\bar{p}p$ annihilation at rest. The $K(E)$ for a few simple channels are also given.

TABLE II. Branching ratios of $\bar{p}p$ annihilation at rest. The decay channels used for Monte Carlo simulation are indicated by asterisks.

Channel	Branching ratio	MC	Reference
$\pi^+\pi^-\pi^0$	0.037	*	35
$\rho^\pm\pi^\mp$	0.027	*	35
$\pi^+\pi^-2\pi^0$	0.093	*	34
$\pi^+\pi^-3\pi^0$	0.233	*	34
$\pi^+\pi^-4\pi^0$	0.028	*	35
$2\pi^+2\pi^-\pi^0(\omega\pi^+\pi^-)$	0.038	*	35
$2\pi^+2\pi^-\pi^0(\rho^0\pi^+\pi^-\pi^0)$	0.073	*	35
$2\pi^+2\pi^-\pi^0(\rho^\pm\pi^\mp\pi^+\pi^-)$	0.064	*	35
$2\pi^+2\pi^-2\pi^0$	0.166	*	34
$2\pi^+2\pi^-3\pi^0$	0.042	*	34
$3\pi^+3\pi^-\pi^0$	0.013	*	35
$\pi^+\pi^-\eta$	0.012		35
$2\pi^+2\pi^-\eta$	0.006		35
$\pi^0\rho^0$	0.014	*	35
$\eta\rho^0$	0.002	*	35
$m\pi^0 (m \geq 2)$	0.032		35
$\pi^+\pi^-$	0.004		34
$2\pi^+2\pi^-$	0.069		34
$3\pi^+3\pi^-$	0.021		34
$KKm\pi (m \geq 1)$	0.024		35

gram.³⁶ To generate ordinary $\bar{p}p$ annihilations, we assumed the branching ratios given in Table II. Baryonium production through $\bar{p}p \rightarrow \gamma B$ was generated by assuming the same decay channels and branching ratios of Table II for B as for $\bar{p}p$ annihilation. The secondary particles were generated according to a Lorentz-invariant phase-space distribution. The three-dimensional production point was simulated according to the experimental vertex distributions (see Fig. 14) approximated in Gaussian forms. The outgoing particles were traced through the detector including the MWPC's, the scintillator hodoscopes, the γ detector, etc. In the γ -ray detector, charged hadrons were treated as minimum-ionizing particles. Electromagnetic showers of γ rays were simulated by using the EGS (Ref. 19) in the following way: we prepared 400 γ -ray samples at each of various energies, taken at increments of 50 MeV between 10 and 1000 MeV. The shower development of each γ ray was stored in a data bank as energy deposits in fine meshes in three-dimensional space within a cylinder of 22 cm in radius and 50 cm in length, independently of actual segmentation of the NaI modules. When a γ ray with a certain energy E was incident on the NaI, a shower was taken randomly from the sample events having an energy closest to E and the energy was scaled to E . The shower axis was put on the incident γ -ray vector after randomly rotating the shower azimuthally. The energy deposit in each NaI module was obtained by summing the fine meshes which belonged to the module.

After the event generation, we simulated the trigger selection condition just as in the actual experiment. We obtained the charge multiplicity by counting hodoscope hits, and the γ -ray multiplicity by counting neutral clus-

ters in the NaI above a threshold of 20 MeV. Then the Monte Carlo event was analyzed with the same reconstruction program as for the real event. For the charged particles, the generated tracks were used for simplicity without reconstruction. This means that the efficiencies of MWPC's were all assumed to be 100% instead of the experimental values of about 95% and that small positional errors in tracking were neglected. This simplification, which is the only difference between real-event and Monte Carlo-event analyses, is expected to give no problem because small errors in tracking are not essential to the γ -ray spectra.

APPENDIX C: REJECTION OF CHARGED PARTICLES FROM γ -RAY SPECTRA

When charged particles, mostly pions, produced in $\bar{p}p$ annihilation hit the NaI, some of them may penetrate it after depositing the minimum-ionization energies there. Figure 25 gives a typical energy-deposit spectrum of charged particles in the NaI constructed from only charged particles that were successfully tracked in the MWPC's. As this spectrum was taken for the whole NaI calorimeter, the injection angles to the NaI were varied. The minimum-ionizing peak is seen at 185 MeV with a FWHM of 22%. If charged particles contaminate γ rays, the minimum-ionizing peak may show up as a fake peak in the γ -ray spectra. We estimate the tolerable upper limit of charged-particle contamination and compare it with the actual performance.

Figure 25 shows that the amount of the minimum-

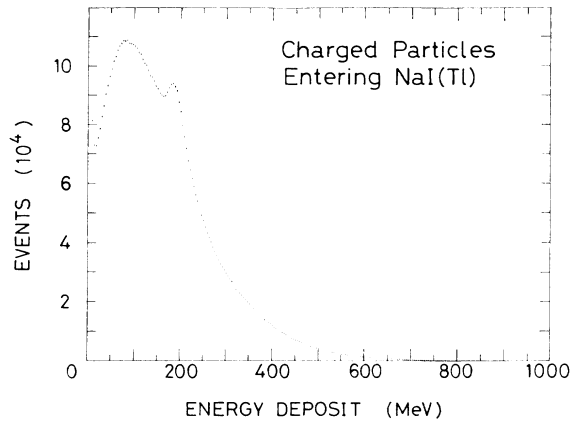


FIG. 25. An energy-deposit spectrum of charged particles in the NaI. Only successfully reconstructed charged particles entering the NaI are included.

ionizing peak was 3% of the total charged particles. When a difference between the multiplicities of charged particles [3.05 (Ref. 27)] and of γ rays [3.93 (Ref. 34)] per annihilation is neglected for simplicity, the charged

particles may fake a γ -ray peak which contains $0.03R_cN_\gamma$ γ rays, where R_c denotes the rejection factor against charged particles. When the above number ($0.03R_cN_\gamma$) is substituted into the peak area A of Eq. (5), the nominal yield of this fake peak is $0.13R_c$. In order to keep the nominal yield below 10^{-4} , the tolerable upper limit for R_c is 8×10^{-4} .

In the actual experiment, an energy deposit in the NaI was taken as a γ ray, only when the following three requirements were satisfied at the same time: (i) absence of a hodoscope hit in front of the hit NaI modules, (ii) absence of a hit wire in C4 in the vicinity of the hit NaI modules, and (iii) absence of any corresponding tracks in cylindrical MWPC's. In (iii), at least two hit planes among four in total were required to indicate a possibility for a track. The rejection factor from (i) is 0.05 from acceptance gaps between neighboring scintillators, that from (ii) is again 0.05 from the inefficiency of wire planes, and that from (iii) is, by taking a contribution independent of (ii), 0.008 from again inefficiencies of wire planes (C1–C3). Multiplying these three numbers, we obtain $R_c = 2 \times 10^{-5}$, which is much smaller than the tolerable upper limit.

*Present address: Kochi Medical School, Nankoku, Kochi 781-51, Japan.

†Present address: Electrotechnical Laboratory, Niihari-gun, Ibaraki-ken 305, Japan.

‡Present address: National Laboratory for High Energy Physics (KEK), Tsukuba-gun, Ibaraki-ken 305, Japan.

¹H. Harari, Phys. Rev. Lett. **22**, 562 (1969); J. L. Rosner, *ibid.* **22**, 689 (1969).

²C. H. Mo and H. Hogaasen, Nucl. Phys. **B136**, 401 (1978); L. Montanet, G. C. Rossi, and G. Veneziano, Phys. Rep. **63**, 149 (1980).

³For a review, see, for example, T. Kamae, in *Proceedings of the Ninth International Conference on High Energy Physics and Nuclear Structure*, Versailles, 1981, edited by P. Catillon, P. Radvanyi, and M. Porneuf [Nucl. Phys. **A374**, 25c (1982)].

⁴I. S. Shapiro, Phys. Rep. **35**, 129 (1978); C. B. Dover, J. M. Richard, and M. C. Zabeck, Ann. Phys. (N.Y.) **130**, 70 (1980).

⁵B. Richter *et al.*, Phys. Lett. **126B**, 284 (1983).

⁶T. Brando *et al.*, Phys. Lett. **139B**, 133 (1984).

⁷J. P. Ader, B. Bonnierand, and S. Sood, Phys. Lett. **101B**, 427 (1981).

⁸A. Angelopoulos *et al.*, Phys. Lett. **159B**, 210 (1985).

⁹ASTERIX Collaboration, S. Ahmad *et al.*, Phys. Lett. **152B**, 135 (1985).

¹⁰L. Adiels *et al.*, Report No. CERN-EP/86-154, 1986 (unpublished).

¹¹A short description is given in M. Chiba *et al.*, Phys. Lett. B **177**, 217 (1986).

¹²M. Kobayashi *et al.*, Nucl. Instrum. Methods **A245**, 59 (1986).

¹³A single crystal of NaI(Tl) was grown and canned by Bicorn Co., Newbury, Ohio.

¹⁴M. Chiba *et al.*, Nucl. Instrum. Methods **A234**, 267 (1985).

¹⁵SCG1C was manufactured by Ohara Optical Glass Manufacturing Co., Sagamihara, Kanagawa, Japan.

¹⁶M. Kobayashi *et al.*, Nucl. Instrum. Methods **A245**, 51 (1986).

¹⁷M. Kobayashi *et al.*, Jpn. J. Appl. Phys. **24**, 593 (1985).

¹⁸M. Takasaki *et al.*, Nucl. Instrum. Methods **A242**, 201 (1986).

¹⁹R. L. Ford and W. R. Nelson, Report No. SLAC-210, 1978 (unpublished).

²⁰H. Yoshida *et al.* (unpublished).

²¹M. Kobayashi, S. Takano, and Y. Matsumoto, Nucl. Instrum. Methods **224**, 318 (1984).

²²H. Yoshida *et al.* (unpublished).

²³L. Taff, D. Ritchie, and T. Lagerlund, Fermilab Report No. PN-110, 1979 (unpublished).

²⁴K. Amako, S. Inaba, Y. Inagaki, and T. Tsuru, Report No. KEK Exp, Facilities-3, 1976 (in Japanese) (unpublished).

²⁵S. Inaba (private communication).

²⁶F. James and M. Roos, Comput. Phys. Commun. **10**, 343 (1975).

²⁷C. Ghesquiere *et al.*, in *Proceedings of the Symposium on Antinucleon-Nucleon Interactions*, Prague, 1974, edited by L. Montanet (CERN, Geneva, 1974), p. 436.

²⁸T. E. Kalogeropoulos, G. Öngünt, C. Petridou, and G. Tzanakos, Phys. Rev. D **26**, 543 (1982).

²⁹T. Spuller *et al.*, Phys. Lett. **67B**, 479 (1977).

³⁰M. Chiba *et al.* (unpublished).

³¹L. Adiels *et al.*, Phys. Lett. B **182**, 405 (1986).

³²A. Angelopoulos *et al.*, Phys. Lett. B **178**, 441 (1986).

³³D. Bridges *et al.*, Phys. Rev. Lett. **56**, 211 (1986); **56**, 215 (1986); **57**, 1534 (1986).

³⁴G. Backenstoss *et al.*, Nucl. Phys. **B228**, 424 (1983).

³⁵R. Armenteros and B. French, in *Antinucleon-Nucleon Interaction in High Energy Physics*, edited by E. H. S. Burhop (Academic, New York, 1969), Vol. 4, p. 237.

³⁶R. Brun, R. Hagelberg, M. Hansroul, and J. C. Lassalle, Report No. CERN-DD/78/2, 1978 (unpublished).